Inference of Cloud Optical Depth from Aircraft-Based Solar Radiometric Measurements

H. W. BARKER,* A. MARSHAK,+ W. SZYRMER,# A. TRISHCHENKO,@ J.-P. BLANCHET,# AND Z. LI&

*Environment Canada, Downsview, Ontario, Canada
+JCET/UMBC and NASA GSFC, Greenbelt, Maryland
#Université du Québec à Montréal, Montréal, Quebec, Canada
@Canada Centre for Remote Sensing, Ottawa, Ontario, Canada
&University of Maryland at College Park, College Park, Maryland

(Manuscript received 8 May 2001, in final form 1 October 2001)

ABSTRACT

A method is introduced for inferring cloud optical depth τ from solar radiometric measurements made on an aircraft at altitude z. It is assessed using simulated radiometric measurements produced by a 3D Monte Carlo algorithm acting on fields of broken boundary layer clouds generated from Landsat imagery and a cloud-resolving model. The method uses upwelling flux and downwelling zenith radiance measured at two solar wavelengths where atmospheric optical properties above z are very similar but optical properties of the surface–atmosphere system below z differ. This enables estimation of cloud reflectance into nadir for upwelling diffuse flux and, finally, τ above z. An approximate one-dimensional radiative Green's function is used to roughly account for horizontal transport of photons in all, even broken, clouds. This method is compared to its surface-based counterpart and shown to be superior. Most notably, the aircraft-based approach deals easily with inhomogeneous land surfaces, is less susceptible to poor sampling, and need not account for aerosol below z.

The algorithm appears as though it will have little difficulty inferring high-resolution time series of $\tau \lesssim 40$ for most (single layer) clouds. For larger values of τ, biases emerge; particularly, underestimation for the statistically infrequent interiors of cumuliform clouds as photon leakage through cloud sides is not addressed. For the cumuliform and stratiform clouds used here, mean bias errors for retrieved τ are $\sim$1 (or $\sim$15%) and $\sim$0.3 (or $\sim$3%), respectively. For stratiform clouds with textured bases, performance is likely to improve slightly for flights just up from mean cloud base.

1. Introduction

Observational estimates of cloud optical depth τ are sought for many reasons, most of which hinge on the important role played by τ in determining earth's radiation budget and climate (Mitchell et al. 1995). Though satellite estimates of τ can be used to help assess global climate models (Han et al. 1998), they are not perfect (Min and Harrison 1996; Barker et al. 1998; Li et al. 1999) and must be validated independently. Moreover, satellites often provide inadequate sampling for some studies, notably field experiments. The other obvious platforms from which suitable observations can be made are fixed surface sites and aircraft. Estimates of τ from surface-based radiometric measurements are spatially limited but can provide excellent temporal coverage, as well as help validate satellite estimates. Conventional surface-based methods for inferring τ use pyranometer data and a plane-parallel homogeneous radiative transfer model (e.g., Leontyeva and Stamnes 1994; Leontieva et al. 1994; Barker et al. 1998) and are known to work fairly well for overcast only. Barker and Marshak's (2001, referred to hereinafter as BM2001) method for inferring τ from surface data extends Marshak et al.'s (2000) normalized difference cloud index (NDCI) and uses time series of zenith radiances and fluxes measured at two wavelengths that have different local area-averaged surface albedos α_s. While their method was shown to do well for nonovercast clouds, it requires, in addition to spectral α_s, estimates of cloud-base altitude and cloud advection rate. Moreover, like all fixed surface sites, it is at the mercy of advection, inevitable anisotropic biases in cloud structure, and undersampling.

Far fewer attempts have been made to infer τ from aircraft observations than from the surface. For example, Gultepe et al. (2001) used in situ data to estimate mean droplet extinction coefficient β, which was then multiplied by mean cloud geometric thickness deduced by flying above and below cloud. Techniques such as these are, however, subject to much uncertainty and, like the conventional surface method, can be expected to yield just mean τ and work well for extensive planar clouds only.

Corresponding author address: Howard Barker, Meteorological Service of Canada, Cloud Physics Research Division (ARMP), 4905 Dufferin St., Downsview, ON, M3H 5T4, Canada.
E-mail: howard.barker@ec.gc.ca

The primary purpose of this paper is to present an aircraft-based method of inferring τ for planar and broken-cloud conditions that builds on BM2001's surface technique. The advantages that this method has over Barker and Marshak's is that it does not require information about surface albedo and it is less susceptible to poor sampling.

In the second section, the method for inferring τ from aircraft-mounted radiometers is presented. The third section presents data and modeling techniques used to test the proposed method. As this method is based in part on a Green's function formulation of radiative transfer, properties of relevant Green's function are presented in the fourth section. In the fifth section, the method is demonstrated and contrasted against its surface-based counterpart (BM2001). The sixth section addresses the issue of feasibility, and conclusions are drawn in the final section.

2. Model development

This section has two subsections, the first of which presents the theoretical foundation and assumptions behind the retrieval algorithm and parallels that in BM2001. The second discusses additional assumptions and outlines application of the algorithm.

a. Theory

Throughout this paper, all radiometric quantities are normalized by incoming spectral solar flux at either cloud top or the top of the atmosphere. Following from Knyazikhin and Marshak (2000), downwelling radiance $I_\lambda^\downarrow$ at wavelength λ, in direction Ω, at point $r_0 = (x_0, y_0)$, and at altitude z above the ground surface can be expressed as

$$I_\lambda^\downarrow(r_0, \Omega; z) = I_{0\lambda}^\downarrow(r_0, \Omega; z) + \int_R \left[\int_{2\pi^-} |\mu'| I_\lambda^\uparrow(r, \Omega'; z) G_\lambda(r, r_0, \Omega, \Omega'; z)\, d\Omega' \right] dr, \tag{1}$$

where R is the plane parallel to earth at z, $I_{0\lambda}^\downarrow$ is the component of $I_\lambda^\downarrow$ consisting of photons that have not encountered the surface–atmosphere system beneath z, μ' is cosine of zenith angle, and $I_\lambda^\uparrow$ is upwelling radiance at $r = (x, y)$. Also, G_λ is a radiative Green's function describing the transfer of upwelling photons at (r, z) traveling in direction Ω' into downwelling photons at (r_0, z) in direction Ω. Limiting downwelling radiances to the nadir direction hereinafter, and defining a radiance-weighted Green's function as

$$G_\lambda(r, r_0; z) = \frac{\displaystyle\int_{2\pi^-} |\mu'| I_\lambda^\uparrow(r, \Omega'; z) G_\lambda(r, r_0, \Omega'; z)\, d\Omega'}{\displaystyle\int_{2\pi^-} |\mu'| I_\lambda^\uparrow(r, \Omega'; z)\, d\Omega'} = \frac{\displaystyle\int_{2\pi^-} |\mu'| I_\lambda^\uparrow(r, \Omega'; z) G_\lambda(r, r_0, \Omega'; z)\, d\Omega'}{F_\lambda^\uparrow(r; z)}, \tag{2}$$

where $F_\lambda^\uparrow(r; z)$ is upwelling flux, (1) can be rewritten as

$$I_\lambda^\downarrow(r_0; z) = I_{0\lambda}^\downarrow(r_0; z) + \int_R F_\lambda^\uparrow(r; z) G_\lambda(r, r_0; z)\, dr. \tag{3}$$

The function G_λ describes the transfer of all upwelling photons at (r, z) into nadir-directed photons at (r_0, z). Figure 1 shows a schematic illustration of (3). Not only does $I_{0\lambda}^\downarrow$ depend much on illumination geometry and cloud structure, it is also a multivalued function of cloud optical depth τ; even for homogeneous clouds (see Fig. 1 in BM2001). Combining these factors makes $I_{0\lambda}^\downarrow$ undesirable for retrieving τ. As such, NDCI (Marshak et al. 2000), BM2001's method, and the method presented here avoid it.

If $I_\lambda^\uparrow$, and hence $F_\lambda^\uparrow$, are independent of r, (3) becomes

$$I_\lambda^\downarrow(z) = I_{0\lambda}^\downarrow(z) + F_\lambda^\uparrow(z) \int_0^\infty G_\lambda(s; z)\, ds, \tag{4}$$

where

$$s = |r - r_0|. \tag{5}$$

This corresponds to the classic 1D scenario: a plane-parallel, homogeneous atmosphere above a uniform, though not necessarily Lambertian, surface. Going further and assuming that $I_\lambda^\uparrow$ is isotropic, simplifies (2) as (cf. Knyazikhin and Marshak 2000)

$$\mathbb{G}_\lambda(s; z) = \frac{I_\lambda^\uparrow(z)}{F_\lambda^\uparrow(z)} \int_{2\pi^-} |\mu'| G_\lambda(s, \Omega'; z)\, d\Omega' = \frac{1}{\pi} \int_{2\pi^-} |\mu'| G_\lambda(s, \Omega'; z)\, d\Omega'. \tag{6}$$

Thus, (4) becomes

$$I_\lambda^\downarrow(z) = I_{0\lambda}^\downarrow(z) + F_\lambda^\uparrow(z) \rho_\lambda(z), \tag{7}$$

where

$$\rho_\lambda(z) = \int_0^\infty \mathbb{G}_\lambda(s; z)\, ds \tag{8}$$

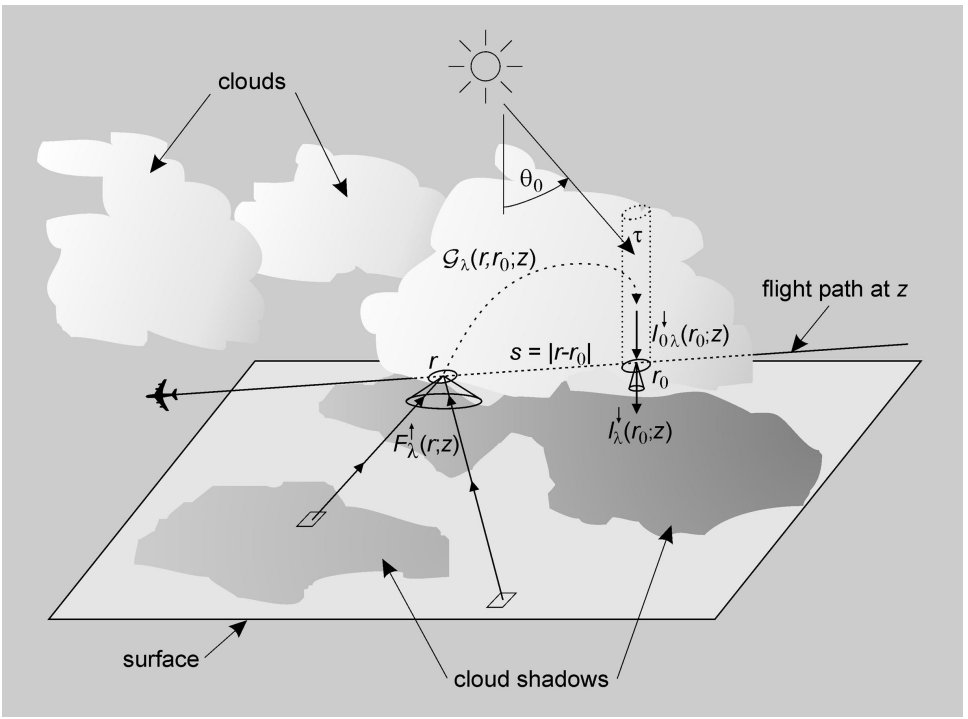

FIG. 1. Schematic illustration of components making up zenith radiance $I^{\downarrow}_{\lambda}(r_0; z)$ measured at r_0 at altitude z. $I^{\downarrow}_{0\lambda}(r_0; z)$ consists of photons that have not been beneath z; $F^{\uparrow}_{\lambda}(r; z)$ are measured upwelling fluxes at r made up of photons that have been beneath z; and $G_{\lambda}(r, r_0; z)$ is a Green's function that describes the fraction of $F^{\uparrow}_{\lambda}(r; z)$ that contributes to $I^{\downarrow}_{\lambda}(r_0; z)$.

is normal reflectance of the atmosphere above z for isotropic upwelling flux and links 1D and 3D radiative transfer theory.

The first two key assumptions of the method presented here are (i) $I^{\uparrow}_{\lambda}$ can be approximated by isotropic upwelling radiance, and (ii) mean horizontal transport of upwelling radiation can be approximated by 1D theory. This implies that

$$\int_R G_{\lambda}(r, r_0; z)\, dr \approx \int_0^{\infty} \mathbb{G}_{\lambda}(s; z)\, ds = \rho_{\lambda}(z), \quad (9)$$

which enables (3) to be approximated as

TABLE 1. Properties of the cloud fields shown in Figs. 2 and 3: A_c is vertically projected cloud fraction; $\langle\tau\rangle$ and $\tau_{\max}$ are mean and maximum cloud optical depths; $\eta = e^{\langle \ln \tau\rangle}/\langle\tau\rangle$, which provides a measure of horizontal variability (Cahalan et al. 1994). Minimum cloud optical depth was 0.01. Here, $\langle z_{\text{top}}\rangle$ and $\langle z_{\text{base}}\rangle$ are mean cloud-top and cloud-base altitudes, and Δz is cloud geometric thickness (km).

	Scene A	Scene B
A_c	0.44	0.89
$\langle\tau\rangle$	6.48	13.23
$\tau_{\max}$	83.2	40.5
η	0.28	0.75
$\langle z_{\text{top}}\rangle$	1.149	1.367
$\langle z_{\text{base}}\rangle$	1.00	1.033
$\langle\Delta z\rangle$	0.149	0.334
$\sqrt{\langle\Delta z^2\rangle}$	0.209	0.352

$$I^{\downarrow}_{\lambda}(r_0; z) \approx I^{\downarrow}_{0\lambda}(r_0; z) + \left\{\int_R F^{\uparrow}_{\lambda}(r; z)\left[\frac{G_{\lambda}(r, r_0; z)}{\int_R G_{\lambda}(r', r_0; z)\, dr'}\right] dr\right\} \times \rho_{\lambda}(\tau(r_0; z)), \quad (10)$$

where $\rho_{\lambda}(\tau; z)$ is assumed to depend only on τ above r_0, which is in turn defined as

$$\tau(r_0; z) = \int_z^{z_{\text{top}}} \beta(r_0; z')\, dz', \quad (11)$$

where β is cloud extinction coefficient, and z_{top} is cloud top altitude. For simplicity, spectral dependencies of τ and β are omitted (though recognized through ρ_{λ}). By defining a normalized Green's function as

$$H_{\lambda}(r, r_0; z) = \frac{G_{\lambda}(r, r_0; z)}{\int_R G_{\lambda}(r', r_0; z)\, dr'}, \quad (12)$$

(10) can be rewritten as

$$I^{\downarrow}_{\lambda}(r_0; z) \approx I^{\downarrow}_{0\lambda}(r_0; z) + \left[\int_R F^{\uparrow}_{\lambda}(r; z) H_{\lambda}(r, r_0; z)\, dr\right] \rho_{\lambda}(\tau(r_0; z)). \quad (13)$$

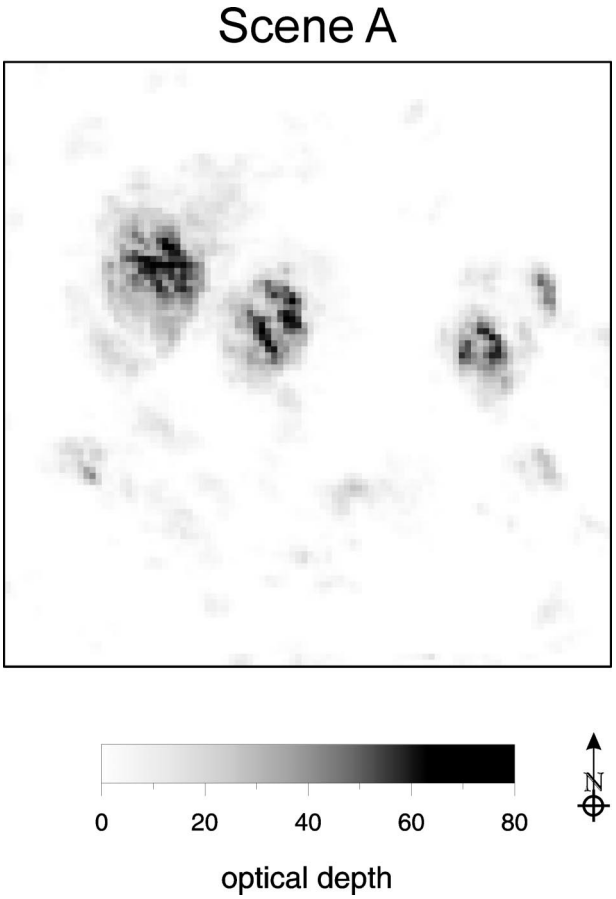

FIG. 2. Optical depth inferred from Landsat imagery for a single layer, marine boundary layer cloud field. Horizontal grid spacing is 114 m and the domain is $(11.4\ \text{km})^2$. In the Monte Carlo simulations, the sun shone in at $\theta_0 = 40°$ from the bottom of the plot (i.e., from the south, as indicated). See Table 1 for scene information.

This approximation for downwelling nadir radiance at r_0 and altitude z forms the basis of the cloud optical depth retrieval algorithm that is developed in the following section.

b. Application

The third key assumption of the method presented here is that measurements of $I_\lambda^\downarrow$ and $F_\lambda^\uparrow$, made on an aircraft at altitude z, are at two wavelengths where atmospheric optical properties above z are very similar but local area-average optical properties of the surface–atmosphere system below z differ. These conditions are satisfied well for green vegetated surfaces at λ of ~0.65 and ~0.87 μm (e.g., Tucker 1979; Verstraete and Pinty 1996). At 0.65 μm, absorption by chlorophyll is strong while at 0.87 μm it is virtually nil. Yet, cloud and aerosol optical properties do not vary much over such a small range of λ, and at these wavelengths gaseous absorption is weak.

Given that ρ_λ is a one-to-one function of τ and is independent of solar zenith angle θ_0, it provides a more direct route to local τ than either $I_\lambda^\downarrow$, $I_{0\lambda}^\downarrow$,or $F_\lambda^\downarrow$. Therefore, evaluating (13) at these λ, taking the difference, and assuming that all quantities that depend exclusively on the atmosphere above z (i.e., τ and thus, $I_{0\lambda}^\downarrow$, ρ_λ, and H_λ) are independent of λ, ρ can be approximated by

$$\rho(\tau(r_0; z)) \approx \frac{I_{\lambda_2}^\downarrow(r_0; z) - I_{\lambda_1}^\downarrow(r_0; z)}{\int_R [F_{\lambda_2}^\uparrow(r; z) - F_{\lambda_1}^\uparrow(r; z)]H(r, r_0; z)\, dr}. \tag{14}$$

Since H is unknown, yet is known to depend on cloud structure, it can be set initially to

$$H(r, r_0; z) = H_\delta(r, r_0; z) \equiv \delta(|r - r_0|), \tag{15}$$

which affects an independent pixel calculation and reduces (14) to

$$\rho(\tau(r_0; z)) \approx \frac{I_{\lambda_2}^\downarrow(r_0; z) - I_{\lambda_1}^\downarrow(r_0; z)}{F_{\lambda_2}^\uparrow(r_0; z) - F_{\lambda_1}^\uparrow(r_0; z)}. \tag{16}$$

These values, along with estimates of droplet asymmetry parameter g and single-scattering albedo ω_0, are then used to make first-order estimates of τ via bisectional root finding with the 1D Discrete Ordinate Radiative Transfer (DISORT) model (Stamnes et al. 1988). Hereinafter, estimates of τ are denoted as τ' (inferred values of τ were limited to $\tau' < 75$). For the present purpose, DISORT used 16 streams and the Henyey–Greenstein (HG) phase function (Henyey and Greenstein 1941). The HG function is adequate, despite use of radiances, because the diffuse backscatter function, the inverse of which is related to ρ, is fairly insensitive to phase function details (Wiscombe and Grams 1976; Barker 1995).

The series of τ' can then be used to define a more realistic H for use in a modified version of (14) defined by

$$\rho(\tau(r_0; z)) \approx \frac{I_{\lambda_2}^\downarrow(r_0; z) - I_{\lambda_1}^\downarrow(r_0; z)}{\int_L [F_{\lambda_2}^\uparrow(r; z) - F_{\lambda_1}^\uparrow(r; z)]\tilde{H}(|r - r_0|; z)\, dr}, \tag{17}$$

where L is the aircraft's trajectory, and $\tilde{H}$ is the integral of H around an annulus of radius $|r - r_0|$ centered on r_0. Here, it is assumed that the integral over R in (14) is approximated well by the integral along L in (17). Thus, a refined series of ρ is produced whose value at the jth point is

$$\rho(\tau(r_j; z)) \approx \frac{I_{\lambda_2}^\downarrow(r_j; z) - I_{\lambda_1}^\downarrow(r_j; z)}{\sum_{k=j-n}^{j+n} [F_{\lambda_2}^\uparrow(r_k; z) - F_{\lambda_1}^\uparrow(r_k; z)]\tilde{H}(|r_k - r_j|; z)}, \tag{18}$$

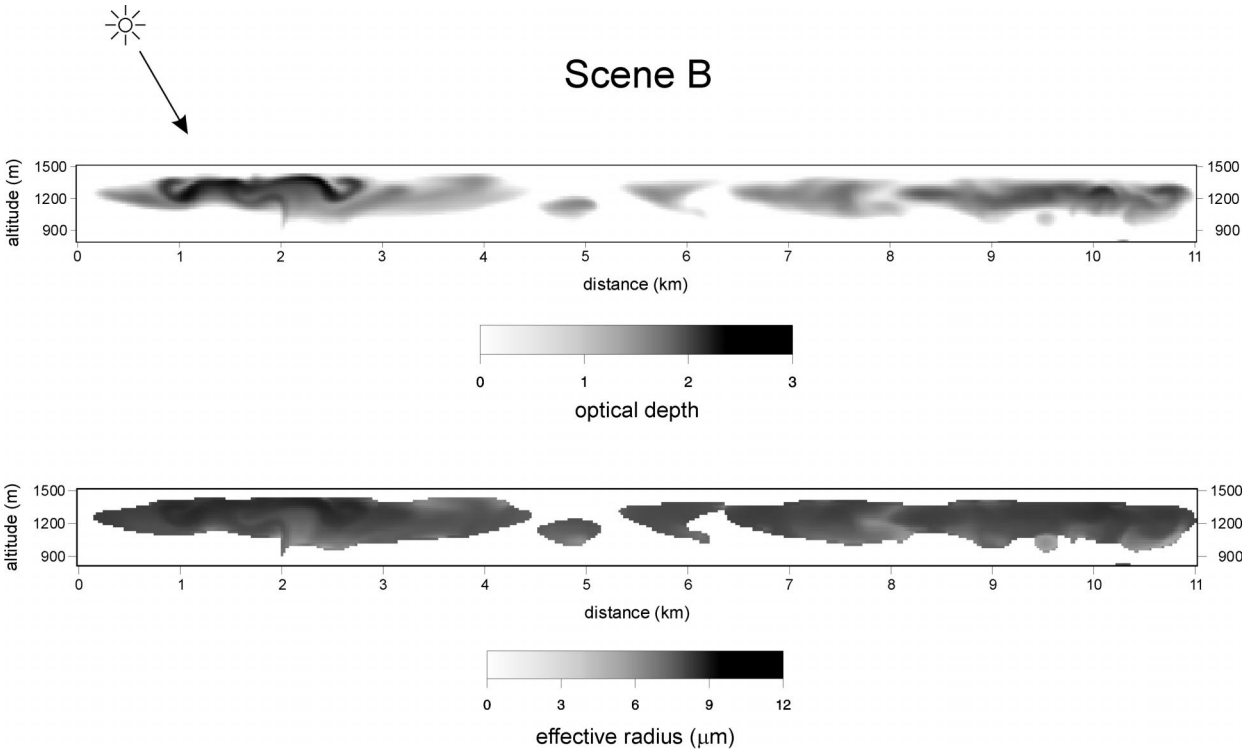

FIG. 3. Profiles of optical depth and droplet effective radius in each cell for an 11-km stretch near the center of Scene B, which measures 100 km long and was simulated by a cloud-resolving model (Szyrmer and Zawadzki 1999). Horizontal and vertical grid spacings are 25 m. Some cloud did exist below 850 m (the lower limit of this plot) though not over this stretch. In the Monte Carlo simulation, the sun shone from the left, as indicated on the plots. See Table 1 for scene information.

TABLE 2. Spectral surface albedos used to create albedo maps for the (11.4 km)^2 area around the ARM-SGP central facility (see Fig. 4). Here, f is fractional area occupied by a Landsat surface type. When albedos are weighed by their respective f and summed, domain-average values at 0.65 and 0.87 μm are 0.090 and 0.381, respectively. Albedo data were collected during Mar 2000 with the portable S2000/PC2000 spectrometer (Ocean Optics Inc.). The spectrometer was equipped with a cosine-corrected fiber optic flux sensor.

Landsat surface type	0.65 μm	0.87 μm	f
Alfalfa	0.063	0.412	0.011
Bare soil	0.126	0.190	0.075
Corn	0.128	0.242	0.054
Pasture, grazed	0.153	0.348	0.138
Legume	0.128	0.242	0.057
Pasture, ungrazed	0.153	0.348	0.120
Trees	0.138	0.306	0.008
Urban	0.136	0.260	0.018
Water	0.050	0.050	0.005
Wheat stubble	0.024	0.501	0.327
Bare ground with wheat stubble	0.024	0.501	0.094
Bare ground with green vegetation	0.138	0.306	0.078
Shrubs	0.138	0.306	0.011
Sand and quarries	0.126	0.190	0.001
Outcrops	0.126	0.190	0.004

where n measurements on either side of the jth point are employed. These values are used, once again, in the DISORT root-finding routine thereby yielding a refined series of τ'. Though ρ and τ' could, in principle, be refined repeatedly, a single iteration was found to be sufficient. Section 4 is devoted to analyzing a viable form of $\tilde{H}$ defined by a gamma distribution.

3. Experimental setup

a. Radiative transfer calculations

A 3D Monte Carlo photon transport algorithm employing cyclic horizontal boundary conditions was used to compute $F_\lambda^\uparrow$ and $I_\lambda^\downarrow$ via the local estimation method (Marchuk et al. 1980). Scattering by air molecules and aerosols was neglected. As discussed in section 2b, the inversion algorithm is concerned primarily with diffuse upwelling fluxes, so detailed descriptions of cloud droplet phase functions are unnecessary. Therefore, to reduce computation time, the HG phase function was used in the Monte Carlo code to represent scattering by very weakly absorbing droplets.

b. Cloud fields

The method described above is illustrated for two fields of broken clouds. Some key statistics for both

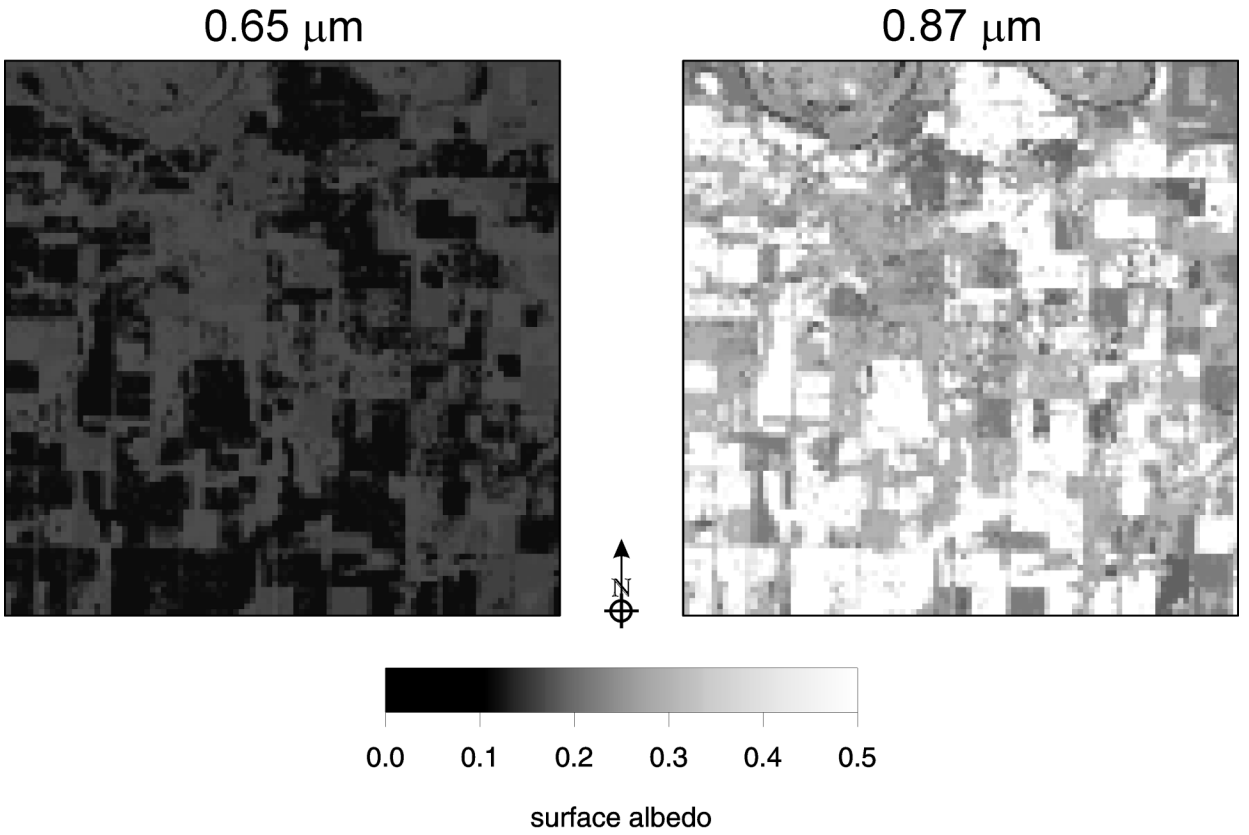

FIG. 4. Surface albedos used for experiments involving Scene A. These (11.4 km)^2 fields are centered on the ARM-SGP central facility (36°36′18″N, 97°29′06″W) and were concocted from Landsat surface classification and measurements made at the surface during Mar 2000 (see Table 2).

fields are listed in Table 1. The first field's optical depths were inferred from 28.5-m resolution Landsat imagery assuming a droplet effective radius r_e of 10 μm (Harshvardhan et al. 1994) for a domain measuring 11.4 km^2. To reduce computational burden, horizontal resolution was degraded to 114 m. This altered the field minimally as radiative smoothing (Marshak et al. 1995a) had already attenuated much of the variability below ~100 m. Figure 2 shows that Scene A is dominated by a few large clouds with a maximum τ of ~83. Cloud-base altitude z_{base} was set to 1 km across the field. Cloud-top altitude (in meters) was defined for each column as

$$z_{\text{top}} = z_{\text{base}} + 45.2\tau^{2/3}, \tag{19}$$

which approximates the Minnis et al. (1992) empirical relation for the range of τ encountered here. Cloud in each column was assumed to be horizontally and vertically homogeneous while vertical resolution is 50 m. Asymmetry parameter g was set to 0.85 everywhere.

It is likely that vertical homogeneity of clouds in Scene A complicates the retrieval process for many simulated flightpaths inside clouds. This is because at any level, more cloud is beneath the plane, masking the surface (see section 6), than would be the case for a cloud with β increasing with altitude (e.g., Stephens and Platt 1987).

The second field, Scene B, was simulated by a 2D, nonhydrostatic cloud-resolving model (Szyrmer and Zawadzki 1999) that employed Brenguier and Grabowski's (1993) microphysical scheme. Vertical and horizontal grid spacings are 25 m and the domain extends from the surface to 1.5 km and is 100 km long; the 2D nature facilitated an extra long transect. For each cell, β, ω_0, and g were determined as a function of liquid water content and r_e using the 0.75–0.78-μm band in Slingo's (1989) parameterization. Figure 3 shows τ and r_e for each cell in an 11-km stretch near the center of the domain. While some cloudy cells are at altitudes as low as 400 m, the vast majority are above 1 km.

It is worth noting that algorithmic performance is likely to be enhanced by the 2D nature of the clouds in Scene B. Since the clouds are fairly planar, however, this is likely to be minor.

c. Surface albedo fields

Two fields of surface albedos were used, both of which were assumed to be Lambertian. The first field

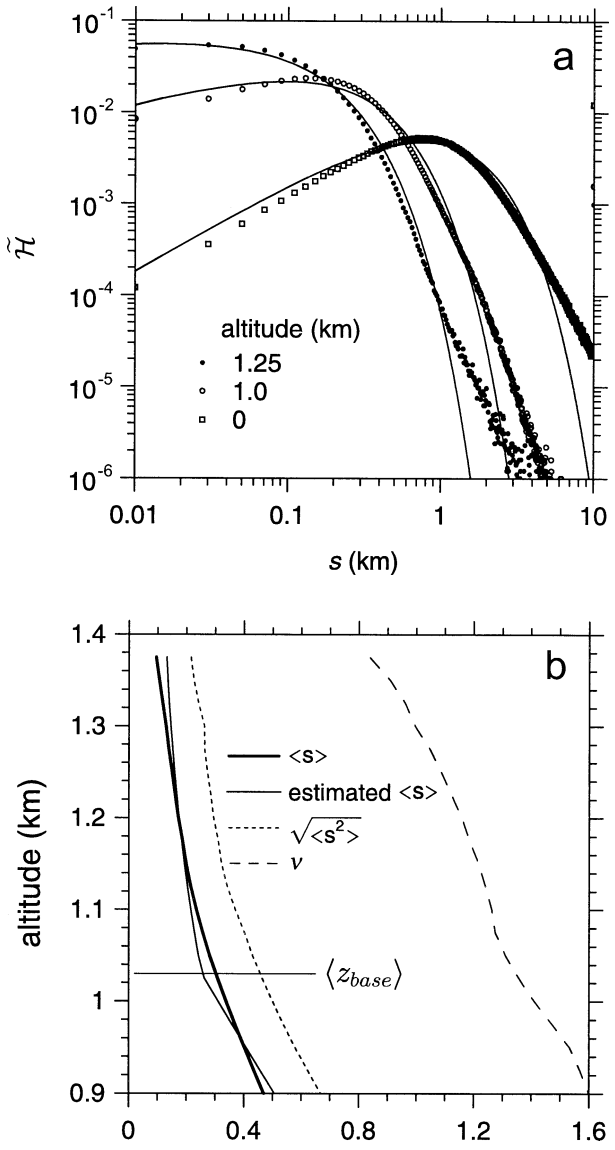

FIG. 5. (a) Points represent normalized frequency distributions of horizontal distance s between entry points of upwelling photons, at altitudes as listed, and downwelling exit points. These were generated by a Monte Carlo algorithm injecting horizontally uniform distributions of upwelling isotropic photons at a particular altitude in Scene B and thus represent horizontally averaged, normalized Green's functions $\tilde{H}$. Solid lines are fitted curves as defined in (21). (b) Vertical profiles of parameters in (21). Also shown is the approximate form of mean entry-to-exit point distance $\langle s \rangle$ estimated by (24).

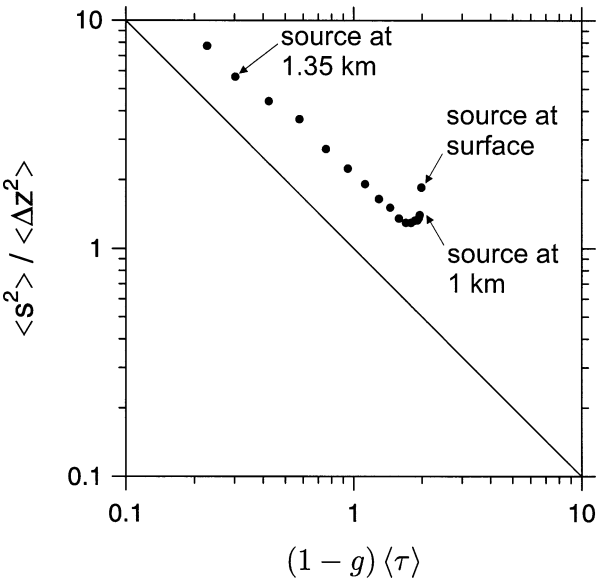

FIG. 6. This plot was constructed using $\langle s^2 \rangle$ as plotted in Fig. 5b, mean square distance between aircraft [referred to here as *source* (i.e., photon injection altitude)] and cloud top $\langle \Delta z^2 \rangle$, $g = 0.85$, and mean cloud optical depth $\langle \tau \rangle$ above aircraft. A straight line of slope -1 corresponds to diffusion (Marshak et al. 1995a; Davis et al. 1997). The deviation from this line for altitudes less than ~1.1 km indicates a break from diffusion.

was homogeneous with albedos of 0.1 and 0.5 representing wavelengths ~0.65 and ~0.87 μm. This field was used for Scene B. The second was used with Scene A and is based on data collected near the Atmospheric Radiation Measurement (ARM) Program's Southern Great Plains (SGP) site in Oklahoma (Stokes and Schwartz 1994). Land types were obtained from the 28.5-m-resolution Landsat database collected during spring and summer and classified by the U.S. Department of Agriculture Hydrology Lab and archived at the Goddard Space Flight Center-Distributed Active Archive Center (GSFC-DAAC). Albedos corresponding to wavelengths 0.65 and 0.87 μm were assigned, based on spectral surface measurements made during March 2000 (see Table 2). Figure 4 shows a marked contrast between these albedos. This is because much of the domain was covered by very young, green vegetation (e.g., Kimes 1983; Kimes et al. 1986; Myneni and Asrar 1993; Lyapustin 1999). Domain-averaged albedos and standard deviations at these wavelengths are 0.090 ± 0.049 and 0.381 ± 0.091, respectively. The fact that the maps in Fig. 4 are only first-order estimates of conditions around the SGP central facility is irrelevant for the present application. Nevertheless, it is interesting to note that one- and two-point statistics of the fields shown in Fig. 4 can be captured extremely well by a 2D cascade model with spectral exponent -1 (see Marshak et al. 1995b for details).

4. Normalized Green's function

The purpose of this section is to provide an approximate, yet simple, means of using H in (17) and (18). In general, $\tilde{H}$ can be expected to be a complicated, spatially variable function of cloud structure. Therefore, for tractability, only horizontal averages of $\tilde{H}$ are considered hereinafter and used in (18). Some characteristics of $\tilde{H}$ are presented here for Scene B.

Estimates of $\tilde{H}$ were obtained with the Monte Carlo algorithm by irradiating cloud at altitude z with a hor-

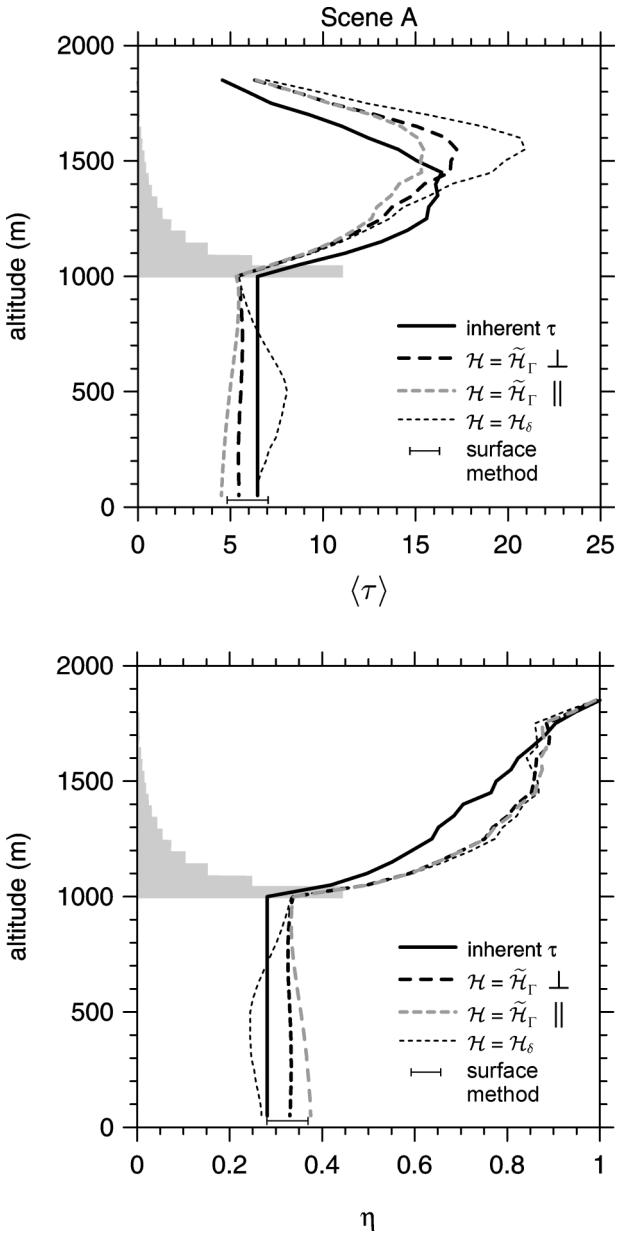

FIG. 7. (Upper panel) Shows profiles of mean optical depth τ inherent to Scene A (see Fig. 2) and inferred by applying the method presented here to simulated radiances and fluxes that would have been measured by an aircraft flying at various altitudes and covering the entire domain. Values were inferred using normalized Green's functions defined by H_δ (a Dirac function) and $\tilde{H}_\Gamma$ (a gamma distribution); the latter for transects perpendicular ($\perp$) and parallel ($\|$) to the direction of incident photons. (Lower panel) Shows corresponding values of the parameter η as defined in (26). Ranges of values indicated for the surface method (BM2001) were obtained using surface albedos (see Fig. 4) averaged around measurement sites for radii from ~0.05 to ~6.4 km. Layer cloud fractions are represented by the fractional extent that the shaded region extends across a plot.

izontally uniform isotropic beam of upwelling photons. If $r = (x, y)$ is a photon's starting point and $r_0 = (x_0, y_0)$ is where it exits the z plane in the nadir direction, distance between entry and exit points is

$$s = |r - r_0| = \sqrt{(x - x_0)^2 + (y - y_0)^2}. \quad (20)$$

Figure 5a shows that $\tilde{H}$ can be approximated well by the gamma distribution

$$\tilde{H}(s; z) \approx \tilde{H}_\Gamma(s; z) \equiv \frac{1}{\Gamma(\nu)}\left(\frac{\nu}{\langle s\rangle}\right)^\nu s^{\nu-1} e^{-s\nu/\langle s\rangle}, \quad (21)$$

where $\langle s\rangle$ and ν are parameters. Here, $\langle s\rangle$ is the mean of s, ν is determined based on maximum likelihood estimation, and $\Gamma(\nu)$ is the gamma function. Also, $\tilde{H}_\Gamma$ depends on z because cloud structure, τ above z, and (once below cloud base) distance from photon injection point to cloud base all depend on z too. Figure 5b shows $\langle s\rangle$ and ν as functions of z. For $z \gtrsim 1$ km (i.e., within the cloud), $\langle s\rangle$ and ν resemble those reported by Davis et al. (1997) for both homogeneous and fractal slab overcast clouds with optical and physical dimensions similar to those of Scene B (see their Fig. 12). This, coupled with the accuracy of (21) near the modes, suggests that when integrated horizontally, local radiative transfer for Scene B is quite similar to that predicted by 1D theory. However, the tails of the computed distributions in Fig. 5a more closely resemble a power law than an exponential. This is due to photons jumping from cloud-to-cloud across gaps that are typically ~0.5 km wide.

Another way to show that local radiative transfer resembles 1D theory, on average, is to consider Marshak et al.'s (1995a) relation derived from diffusion theory for plane-parallel clouds. They showed, as did Davis et al. (1997) for planar fractal clouds, that the mean-squared displacement between entry and exit point can be expressed as

$$\langle s^2\rangle \approx c\frac{\Delta z^2}{(1 - g)\langle\tau\rangle}, \quad (22)$$

where Δz is cloud geometric thickness, $\langle\tau\rangle$ is mean cloud optical depth, and c is a proportionality factor (of order 1). For the experiments performed here, Δz^2 in (22) is replaced by mean-square distance from z to cloud top $\langle\Delta z^2\rangle$, and $\langle\tau\rangle$ represents mean cloud optical depth above z. Figure 6 shows $\langle s^2\rangle/\langle\Delta z^2\rangle$ plotted against $(1 - g)\langle\tau\rangle$ for Scene B. From near cloud top at ~1.37 km down to ~1.15 km, agreement is excellent with Davis et al.'s (1997) values for overcast, planar, fractal clouds (see their Fig. 10b) with c typically between 2 and 3. This suggests that for z inside clouds, radiative transfer through Scene B's clouds resembles very much that through homogeneous clouds.

As z decreases below ~1.15 km, an increasing number of photons begin their trajectories beneath cloud base and so can experience long initial lateral jumps (before the first scattering event) that are beyond the

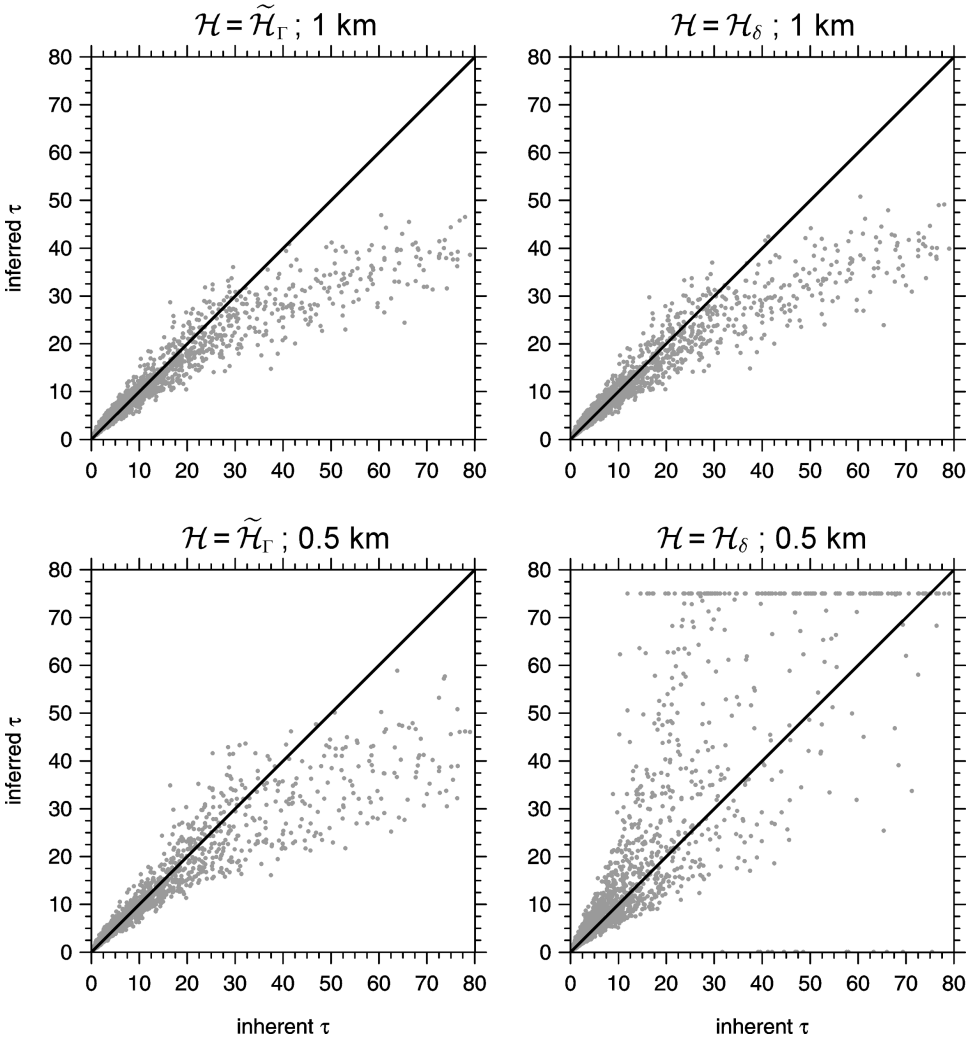

FIG. 8. Scatterplots of inherent τ against τ' inferred by an aircraft at altitudes of 1 and 0.5 km for Scene A using the SGP surface. Inferences are for use of Green's functions $\tilde{H}$ in (18) defined by either H_δ (right panels) or $\tilde{H}_\Gamma$ (left panels).

TABLE 3. Inherent mean optical depth $\langle\tau\rangle$ and variance-related parameter η [see (26)] for clouds in Scene A. Also listed are corresponding values inferred by an aircraft at 1 km (or cloud base) using H_δ (Dirac function) and $\tilde{H}_\Gamma$ (gamma distribution) for ensembles of all flight tracks perpendicular ($\perp$) and parallel ($\parallel$) to the incident solar beam. Results from BM2001's surface-based method are listed too, using spectral surface albedos averaged out to radii of 6.4 km and point values (again for ensembles of all $\perp$ and $\parallel$ transects). MBE and rmse relative to inherent τ are given. Mean cloud spherical albedos $\langle\alpha_{\rm cld}\rangle$ were computed by the independent pixel approximation using the conservative scattering delta-Eddington two-stream approximation with $g = 0.85$.

Method	$\langle\tau\rangle$	η	MBE	Rmse	$\langle\alpha_{\rm cld}\rangle$
Inherent values	6.48	0.28	—	—	0.259
Aircraft at 1 km; H_δ	5.45	0.33	−1.03	4.90	0.258
Aircraft at 1 km; $\tilde{H}_\Gamma$; $\perp$	5.38	0.34	−1.10	5.10	0.257
Aircraft at 1 km; $\tilde{H}_\Gamma$; $\parallel$	5.33	0.34	−1.15	5.18	0.256
Surface; $\langle\alpha_s\rangle$ for 6.4 km; $\perp$	5.87	0.33	−0.61	6.39	0.264
Surface; $\langle\alpha_s\rangle$ for 6.4 km; $\parallel$	4.90	0.37	−1.58	6.61	0.249
Surface; point values of α_s; $\perp$	6.78	0.28	0.29	9.94	0.265
Surface; point values of α_s; $\parallel$	6.67	0.28	0.19	9.86	0.261

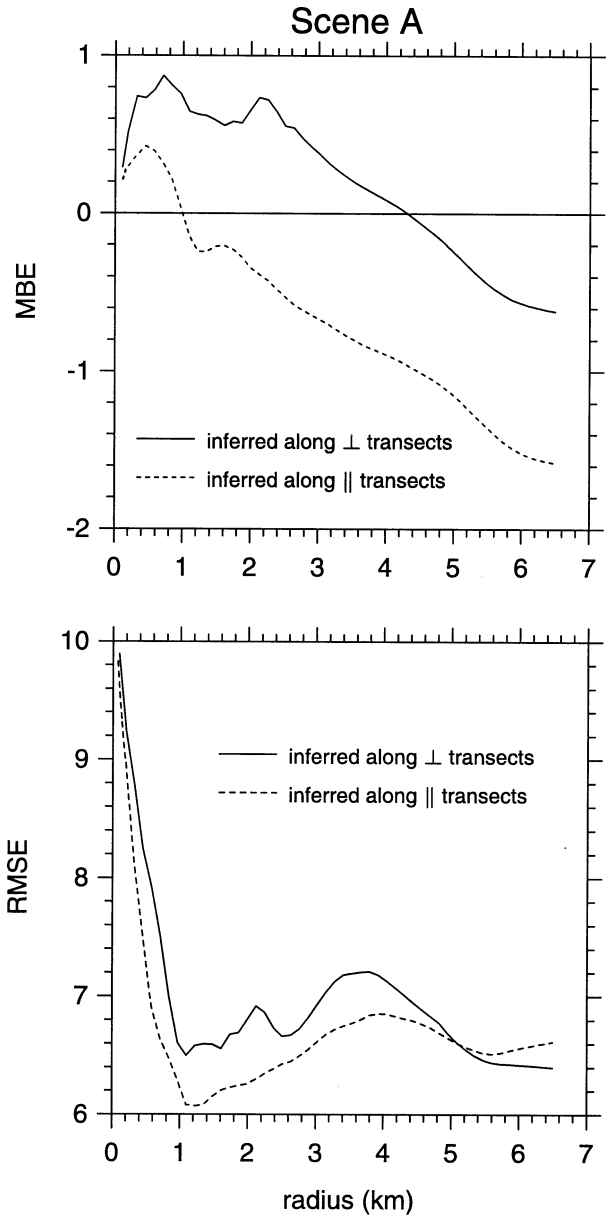

FIG. 9. MBE (upper) and rmse (lower) for τ retrieved by BM2001's surface-based method as a function of surface albedo averaging radius for Scene A using the SGP surface. Values at the extreme left correspond to use of point albedos in (27a) while those at the extreme right used albedos averaged over almost the entire domain. Results are shown for transects both ⊥ and ∥ to the direction of incident photons.

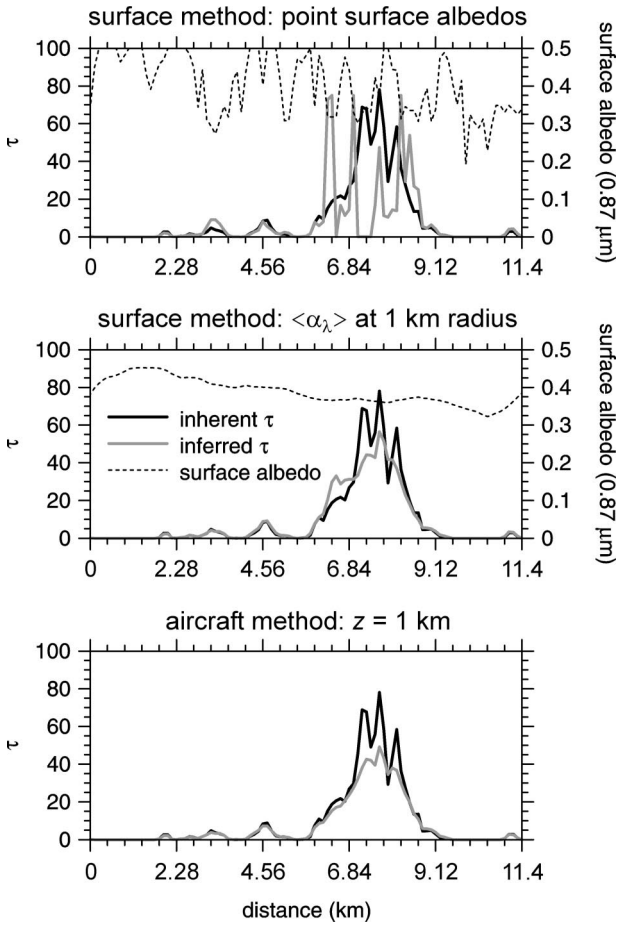

FIG. 10. Top two panels show inherent τ, τ' inferred using BM2001's surface method, as well as surface albedos at 0.87 μm used by the surface method. This is a N–S transect about 25% of the way across Scene A (see Fig. 2). Uppermost panel used point surface albedo values while the middle panel used values averaged within 1 km of measurement sites. Lower panel shows inherent τ and τ' inferred with the aircraft method for a plane flying at 1 km. The Green's function was represented by $\tilde{H}_\Gamma$.

realm of diffusion. By the time the injection level is at the surface ($z = 0$), long initial lateral jumps significantly boost $\langle s^2 \rangle$, and thus $\langle s^2 \rangle / \langle \Delta z^2 \rangle$, thereby signifying a radical departure from the diffusion domain. BM2001 dealt with this anomalous diffusive aspect by simple geometric ray tracing from surface to cloud base. This is evident in Fig. 5a as well: at $z = 0$, the mode of $\tilde{H}_\Gamma$ occurs at $s \approx 1$ km with $\langle s \rangle \approx 1.6$ km and $\nu \approx 2$.

Using the method of moments, $\langle s^2 \rangle = [(1 + \nu)/\nu]\langle s \rangle^2$ for (21), which when substituted into (22) with $c \approx 2$, yields

$$\langle s \rangle \approx \sqrt{\left(\frac{2\nu}{1 + \nu}\right)\frac{\langle \Delta z^2 \rangle}{(1 - g)\langle \tau \rangle}} \tag{23a}$$

for z very close to mean cloud-base altitude $\langle z_{\text{base}} \rangle$ (1.03 km for Scene B) or inside cloud. Figure 5b shows that ν is typically between 0.8 and 1.2 at these altitudes so (23a) can be approximated well by

$$\langle s \rangle \approx \sqrt{\frac{\langle \Delta z^2 \rangle}{(1 - g)\langle \tau \rangle}}. \tag{23b}$$

For isotropic upwelling flux at $z < \langle z_{\text{base}} \rangle$ with clear lines of sight between z and $\langle z_{\text{base}} \rangle$, mean initial lateral

displacements are $2(\langle z_{\text{base}}\rangle - z)$ (along a mean slant path of zenith angle 60°). Thus, assuming that $\langle \Delta z^2\rangle \approx \langle \Delta z\rangle^2$ (see Table 1), where $\langle \Delta z\rangle$ is distance between mean cloud-top altitude $\langle z_{\text{top}}\rangle$ and the aircraft at z:

$$\langle s\rangle \approx \begin{cases} \dfrac{\langle \Delta\rangle}{\sqrt{(1-g)\langle\tau\rangle}}; & \langle z_{\text{base}}\rangle \le z < \langle z_{\text{top}}\rangle \\ \underbrace{\dfrac{\langle z_{\text{top}}\rangle - \langle z_{\text{base}}\rangle}{\sqrt{(1-g)\langle\tau\rangle}}}_{\text{diffusion}} + \underbrace{2(\langle z_{\text{base}}\rangle - z)}_{\text{anomalous diffusion}}; & 0 < z < \langle z_{\text{base}}\rangle, \end{cases} \tag{24}$$

where flights beneath $\langle z_{\text{base}}\rangle$ have distinct contributions from diffusive and anomalous diffusive trajectories. Figure 5b shows (24) plotted against corresponding Monte Carlo values. For z through the entire cloud, and for a fair distance beneath $\langle z_{\text{base}}\rangle$, (24) agrees extremely well with Monte Carlo values. As results are not too sensitive to ν, it is safe to use simply

$$\nu \approx \begin{cases} 1; & \langle z_{\text{base}}\rangle \le z < \langle z_{\text{top}}\rangle \\ 1.5; & 0 < z < \langle z_{\text{base}}\rangle. \end{cases} \tag{25}$$

Note that for $\nu = 1$, (21) reduces to the single-parameter exponential distribution. To apply (24) and (25), estimates of $\langle z_{\text{base}}\rangle$ and $\langle z_{\text{top}}\rangle$ must be available (e.g., from cloud profiling radar or lidar). The majority of results reported hereinafter follow from use of H_δ in (16) followed by $\tilde{H}_\Gamma$ in (18) with parameters estimated by (24) and (25). Some results, however, are shown for when the process is cut short at only (16).

Monte Carlo–derived estimates of $\tilde{H}$ for Scene A (not shown) indicated that for altitudes near $\langle z_{\text{base}}\rangle$, $\tilde{H}_\Gamma$ is often insufficient; photon jumps from cloud-to-cloud are too prevalent. Nevertheless, (24) and (25) were applied to Scene A, but to be truly useful, a more sophisticated approach is needed for sparse cloud fields with well-defined 3D structure.

5. Cloud optical depth retrievals

The simulations reported here used θ_0 of 40° for Scene A and 30° and 60° for Scene B. For this idealized pilot study, the instruments were assumed to be perfect (Monte Carlo noise being the only source of error). For Scene A, the sun shone from the south (from direction $\uparrow$ in Figs. 2 and 4); other solar azimuth angles were tested and all yielded results similar to those presented. Retrievals were done along transects running parallel and perpendicular to the direction of incident photons (i.e., at solar azimuth angles of 0° $\updownarrow$ 180° and 90° $\leftrightarrow$ 270°). For Scene B, the sun shone from the left (see Fig. 3). Since r_e for Scene B were available, (16) and (18) were solved using g derived from r_e at r_0 (Slingo 1989) when the aircraft was inside cloud. When the aircraft was out of cloud, they were solved using $g = 0.85$.

This section consists of two parts. The main point of the first part is to assess the performance of the aircraft-based method for fairly dense broken clouds and to demonstrate the simplicity of the aircraft-based method relative to its surface-based counterpart (BM2001). This is done using Scene A and the SGP surface. The second part documents the impact of using $\tilde{H}_\Gamma$ to describe $\tilde{H}$ and extends the comparison between aircraft and surface methods.

a. Scene A: Inhomogeneous surface albedo

Figure 7 shows profiles of mean inherent $\langle\tau(z)\rangle$ and inferred $\langle\tau'(z)\rangle$ horizontally averaged cloud optical depth above an aircraft for Scene A over the SGP surface. Profiles of $\langle\tau'(z)\rangle$ were obtained using $\tilde{H}$ defined both by $\tilde{H}_\Gamma$ for flights perpendicular ($\perp$) and parallel ($\parallel$) to the direction of incident photons, and by H_δ. Figure 7 also shows profiles of

$$\eta(z) = \frac{e^{\langle \ln\tau(z)\rangle}}{\langle\tau(z)\rangle}, \tag{26}$$

which is used as an indicator for horizontal variability of τ and τ' (Cahalan et al. 1994). For homogeneous clouds, $\eta = 1$. As clouds become increasingly variable, η decreases towards zero. Note that profiles of $\langle\tau\rangle$ need not be monotonic functions of z since averaging was done for cloudy columns only. In Fig. 7 the general trend is $\langle\tau'\rangle > \langle\tau\rangle$ for flights near cloud top, and $\langle\tau'\rangle < \langle\tau\rangle$ for flights between midcloud and cloud base. For virtually all altitudes, inferred η are too large implying that clouds appear to be less variable than they actually are. While flying $\perp$ or $\parallel$ to incident sun has little impact on τ', it would appear that neglect of the Green's function adjustment has a detrimental effect only near cloud top where cloud is sparse. Figure 8 shows, however, that use of the Green's function can be useful. At 1 km, retrievals are excellent for $\tau \lesssim 30$, and variances of τ' for a given τ are small. At this altitude, the impact of $\tilde{H}_\Gamma$ is small because fluctuations in $F_\lambda^\uparrow$ are small too. While there is a minor tendency to overestimate at $\tau \lesssim$

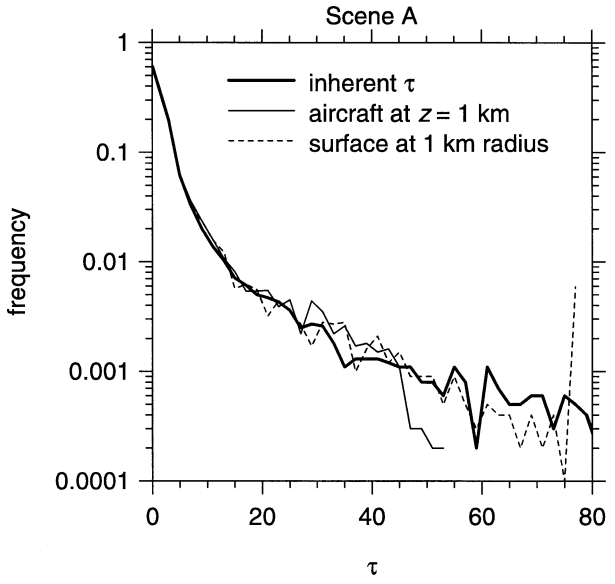

FIG. 11. Frequency distributions of inherent τ for Scene A and τ' inferred by both the aircraft method for a plane at 1 km (using $\tilde{H}_\Gamma$ to describe $\tilde{H}$) and BM2001's surface method using surface albedos averaged within 1 km of measurement sites.

5, there is a marked underestimation for $\tau \gtrsim 30$, which explains the overestimate of η. These biases are due to radiative leakage from dense cores out to thin edges, which makes cores (edges) appear, from a 1D perspective, to be thinner (thicker) than they actually are (e.g., Barker and Li 1997; Marshak et al. 1998). For flights at 0.5 km, the impact of $\tilde{H}_\Gamma$ is clear where almost all the benefit comes from the anomalous diffusion term in (24).

In addition to the aircraft-based retrievals, Fig. 7 also shows results for its close relative, BM2001's surface-based method. In their method, (18) is replaced by

$$\rho(\tau(r_0)) = \frac{I^{\downarrow}_{\lambda_2}(j) - I^{\downarrow}_{\lambda_1}(j)}{\langle\alpha_{\lambda_2}\rangle\tilde{F}^{\downarrow}_{\lambda_2}(j) - \langle\alpha_{\lambda_1}\rangle\tilde{F}^{\downarrow}_{\lambda_1}(j)}, \qquad (27a)$$

where

$$\tilde{F}^{\downarrow}_{\lambda}(j) \approx \frac{\sum_{k=j-n}^{j+n} w(k-j)F^{\downarrow}_{\lambda}(k)}{\sum_{k=j-n}^{j+n} w(k-j)}, \qquad (27b)$$

in which $F^{\downarrow}_{\lambda}(k)$ are the kth measurements in time series of downwelling surface fluxes, and w is a weighting function symmetric about the jth measurement (which corresponds to r_0) and depends on cloud advection rate and $\langle z_{\text{base}}\rangle$. Spectral surface albedos $\langle\alpha_\lambda\rangle$ are mean values around the measurement site. The range of results indicated on Fig. 7 are for $\langle\alpha_\lambda\rangle$ computed as the arithmetic mean of pixel values around measurement sites for averaging radii between ~50 m [single pixels; use of $\alpha_\lambda(j)$ in (27a)] and ~6.5 km (about the entire domain). These plots, and Table 3, which summarizes several retrievals, indicate that the surface- and aircraft-based methods perform comparably, at least as far as means and η are concerned.

Figure 9 shows mean bias error (MBE) and root-mean-square error (rmse) for the surface method as a function of surface albedo averaging radius. It is obvious from the rmse values that very local $\langle\alpha_\lambda\rangle$ (i.e., even those measured atop a 30-m tower) are inappropriate. Root-mean-square errors are minimized for about a ~1-km radius ($\approx\langle z_{\text{base}}\rangle$) and are only about 20% larger than those for the aircraft method at z = 1 km (see Table 3).

Figure 10 shows a sample of τ, τ', and $\langle\alpha_{\lambda_2}\rangle$ along a transect across Scene A. The top panel shows that individual pixel values of α_{λ_2} are quite variable and, when used in (27a), result in excessive τ' when α_{λ_2} are relatively low. This is because the algorithm counters underestimates of upwelling flux at cloud base by overestimating τ (i.e., making clouds more reflective). The middle panel shows that when α_λ are averaged out to 1 km, not only are $\langle\alpha_\lambda\rangle$ fairly smooth, but estimates of τ are much improved. The lower panel shows aircraft inferred τ for a flight at z = 1 km. Since cloud-base flux is now measured directly, much of the random error seen in the upper panels vanishes.

TABLE 4. As in Table 3 except these values are for Scene B with values inferred by an aircraft at two altitudes and by the surface method of BM2001. Inherent values are in parentheses as they depend on aircraft altitude.

Method	$\langle\tau\rangle$	η	MBE	Rmse	$\langle\alpha_{\text{cld}}\rangle$
		$\theta_0 = 30°$			
Aircraft at 1 km; H_δ	12.76 (13.01)	0.73 (0.75)	−0.25	1.81	0.528 (0.537)
Aircraft at 1 km; $\tilde{H}_\Gamma$	12.54 (13.01)	0.74 (0.75)	−0.46	1.57	0.527 (0.537)
Aircraft at 0.5 km; H_δ	14.53 (13.23)	0.68 (0.74)	1.30	5.73	0.538 (0.539)
Aircraft at 0.5 km; $\tilde{H}_\Gamma$	13.09 (13.23)	0.73 (0.74)	−0.14	2.74	0.531 (0.539)
Surface	14.85 (13.23)	0.72 (0.74)	1.62	4.00	0.556 (0.539)
		$\theta_0 = 60°$			
Aircraft at 1 km; H_δ	12.49 (13.01)	0.75 (0.75)	−0.52	1.86	0.526 (0.537)
Aircraft at 1 km; $\tilde{H}_\Gamma$	12.47 (13.01)	0.75 (0.75)	−0.54	1.54	0.526 (0.537)
Aircraft at 0.5 km; H_δ	15.32 (13.23)	0.72 (0.74)	0.11	5.10	0.532 (0.539)
Aircraft at 0.5 km; $\tilde{H}_\Gamma$	13.12 (13.23)	0.73 (0.74)	−0.11	3.19	0.531 (0.539)
Surface	14.45 (13.23)	0.74 (0.74)	1.22	3.43	0.555 (0.539)

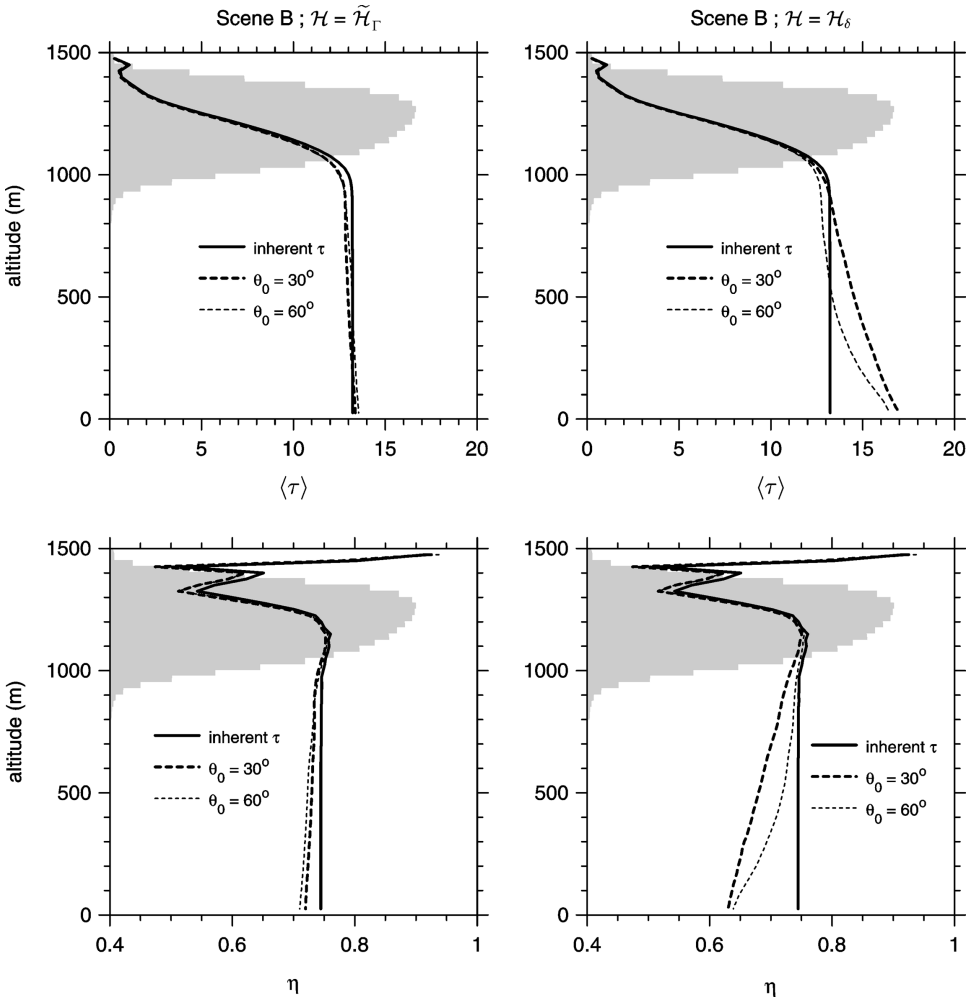

FIG. 12. As in Fig. 7 except these are for Scene B. Inferred values of $\langle\tau\rangle$ (upper panels) and η (lower panels) are for two sun angles θ_0 as listed. Plots on the left are for $\tilde{H}_\Gamma$ while those on the right are for H_δ. Though not visible on this plot, a very small fraction of cloud existed down to ~400 m.

Figure 11 shows normalized frequency distributions $p(\tau)$ for inherent τ and τ' for both the aircraft method at 1-km altitude and the surface method using $\langle\alpha_\lambda\rangle$ averaged out to 1 km around measurement sites. Up to $\tau \approx 40$ both inferred distributions resemble the inherent one extremely well. Then, the aircraft distribution cuts out entirely at $\tau \approx 53$ while the surface distribution registers numerous values topped out at $\tau'_{\max} = 75$ (the maximum admissible τ').

To estimate the impact of these differences in $p(\tau)$ on radiative transfer, mean cloud spherical albedos were computed as

$$\langle\alpha_{\text{cld}}\rangle \equiv \int_0^{\tau_{\max}} p(\tau)\left[2\int_0^1 \alpha(\mu, \tau)\mu\, d\mu\right] d\tau, \quad (28)$$

where $\alpha(\mu, \tau)$ is zenith angle-dependent albedo for a single-layer cloud according to the delta-Eddington two-stream approximation (Joseph et al. 1976). Assuming conservative scattering, $g = 0.85$, and a black surface, $\langle\alpha_{\text{cld}}\rangle$ for inherent $p(\tau)$ is 0.259, for the aircraft $p(\tau')$ it is 0.258, and for the surface $p(\tau')$ it is 0.273 (it would have been slightly larger had $\tau'_{\max}$ been larger than 75). Given that $\langle\alpha_{\text{cld}}\rangle$ for a homogeneous cloud of $\langle\tau\rangle \approx 6.5$ with the same boundary conditions is 0.421, from a domain-averaged flux standpoint, distributions of τ inferred by all methods are extremely good. Values of $\langle\alpha_{\text{cld}}\rangle$ for additional retrievals are listed in Table 3.

To summarize, both the aircraft and surface methods perform very well, the edge going to the aircraft method on account of systematically lower rmse's and slightly more accurate estimates of $\langle\alpha_{\text{cld}}\rangle$.

b. Scene B: The impact of $\tilde{H}$

Figure 12 shows profiles of $\langle\tau\rangle$ and $\langle\tau'\rangle$ and corresponding values of η at $\theta_0 = 30°$ and 60° for Scene B.

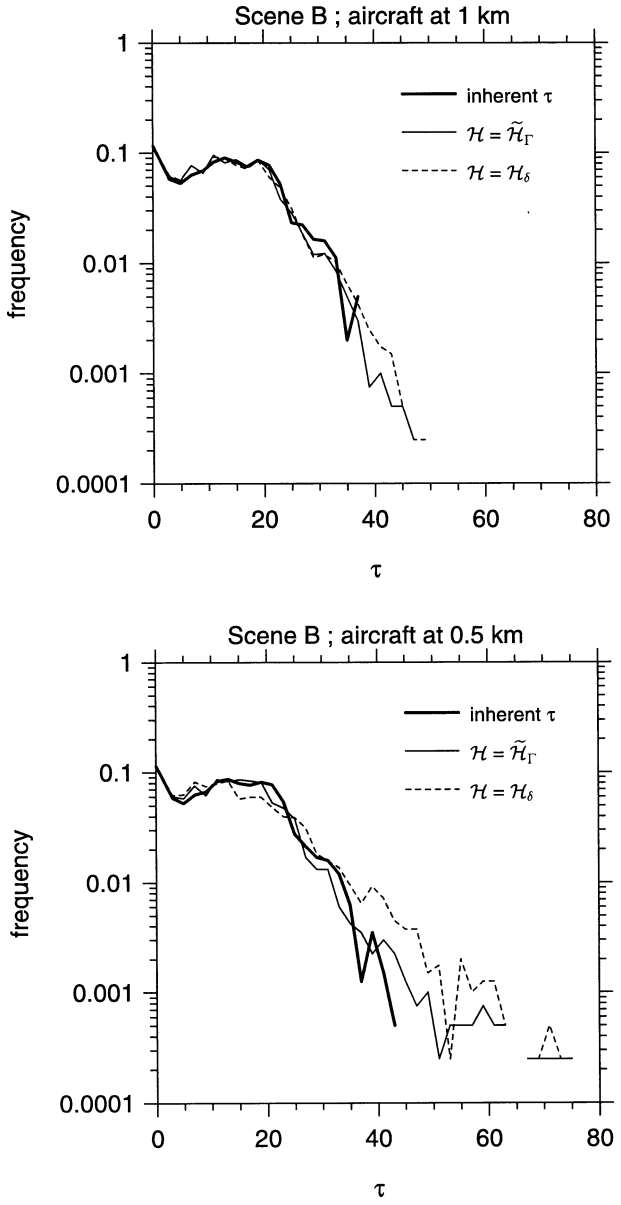

FIG. 13. As in Fig. 9 except these are for Scene B and for aircrafts flying at 1 and 0.5 km in which τ were inferred assuming either $\tilde{H}_\Gamma$ or H_δ to represent $\tilde{H}$ in (18).

For both θ_0, results are excellent for flights above $\langle z_{\text{base}} \rangle \approx$ 1km, regardless of the form of $\tilde{H}$. Table 4, however, shows that in going from $\tilde{H}$ portrayed by H_δ to $\tilde{H}_\Gamma$, rmse's are reduced by ~15%. For flights below $\langle z_{\text{base}} \rangle \approx$ 1 km, it becomes essential that $\langle s \rangle$ in $\tilde{H}_\Gamma$ contain at least the anomalous diffusion term in (24). Moreover, Table 4 indicates that at $z = 0.5$ km, rmse's are approximately halved when $\tilde{H}_\Gamma$ is employed. This impact is also obvious in Fig. 13, which shows frequency distributions of inherent τ and τ' inferred at 1 km and 0.5 km. At 0.5 km the paucity of values near 20 and abundance near 40 that stem from use of H_δ are largely rectified when $\tilde{H}_\Gamma$ is invoked on the second pass. For reference, Table 4 lists results obtained with the surface-based method. While it does not perform as well as the aircraft method (at virtually all altitudes), its relative MBE is still just ~9%.

Figure 14 shows plots of τ' (using $\tilde{H}_\Gamma$) against τ and illustrates what happens to τ' as the aircraft flies from 1 km (approximately $\langle z_{\text{base}} \rangle$) to 1.2 km (inside the main body of cloud; see Fig. 3). Simply going from 1 km to 1.1 km, the rmse decreased by 40% while $\langle \tau \rangle$ decreased by 18%. The improvement in performance comes from avoiding protrusions at cloud base, closer proximity to the diffusion domain, and the appropriateness of using a horizontally averaged Green's function. At an altitude of 1.2 km, only about half the cloud is aloft but the rmse is three times smaller than at 1 km.

Figure 15 provides a closer look at the impact of $\tilde{H}_\Gamma$. It shows τ for a 20-km stretch of Scene B at $\theta_0 = 30°$ as well as τ' inferred using H_δ (initial pass) and $\tilde{H}_\Gamma$ (refined values). For the flight at $z = 1$ km, the initial pass is already excellent but the refined values generally improve performance slightly. At $z = 0.5$ km the initial pass occasionally displays wild excursions away from inherent values. Very often, however, the second pass, with the parameters of $\tilde{H}_\Gamma$ set by the initial pass, rectifies these excursions extremely well; in particular at distances near 9, 11, and 13 km along this stretch. It is important to point out that through use of a horizontally averaged Green's function, the second pass is not, and should not, be expected to always be better than the first. For example, at distances near 10.5 and 16.5 km along the transect, the refined values are slightly worse. Results might improve slightly if parameters in (24) are based on local estimates rather than domain averages.

Notice that for the 0.5-km flight in Fig. 15 the Green's function improves initial estimates most near cloud edges. To understand why, consider Fig. 16, which shows τ and τ' (inferred for a flight at 0.5 km) along with the 6-km stretch of Scene B and its corresponding upwelling fluxes at 0.87 μm. For the sections of flight path labelled **A** and **B**, initial estimates of τ are too small and large, respectively. Refined estimates using $\tilde{H}_\Gamma$ are excellent for both subsections. The lower panel in Fig. 16 shows that because of the proximity of direct-beam surface flux (the explosion of light at ~0.5 km across this transect), $F_\lambda^\uparrow$ measured across **A** are larger than $F_\lambda^\uparrow$ at cloud base directly above. So in order to account for measured $I_\lambda^\downarrow$, the algorithm returns values of τ' that are too small. Use of $\tilde{H}_\Gamma$, however, accounts for smaller $F_\lambda^\uparrow$ along the flight path at the extreme left of the domain and across **B**, which initializes the algorithm with a suitable estimate of $F_\lambda^\uparrow$ at cloud base, and thereby affects good estimates of τ. The reverse is true for measurements taken across **B**. These measured $F_\lambda^\uparrow$ are too small relative to $F_\lambda^\uparrow$ directly above at cloud base and so initial estimates of τ are too large. Use of $\tilde{H}_\Gamma$ captures the large upwelling source measured back at **A**, produces accurate estimates of $F_\lambda^\uparrow$ at cloud base, and thus yields acceptable estimates of τ across **A**.

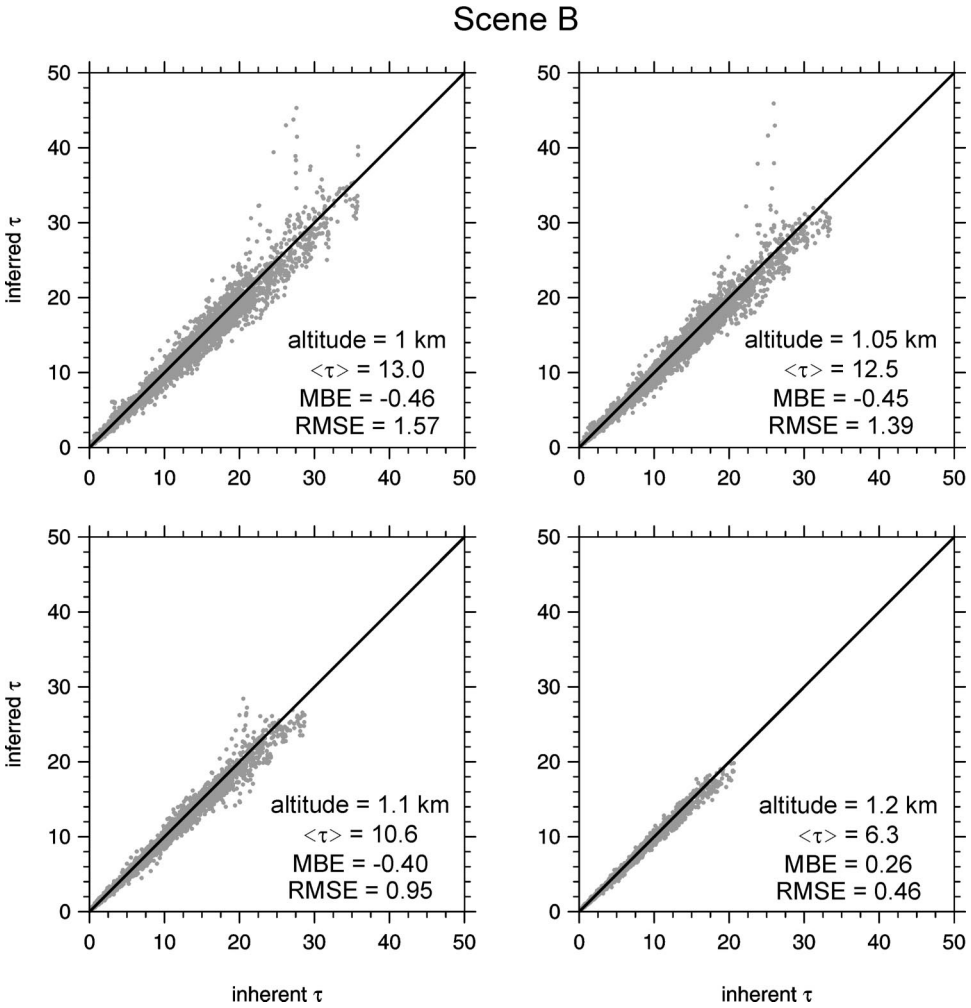

FIG. 14. Scatterplots of inferred τ against inherent τ for Scene B for an aircraft at various altitudes (as indicated on the plots). Also indicated on the plots are mean cloud optical depth above aircraft $\langle\tau\rangle$, MBE, and rmse. Values of τ' were inferred using $\tilde{H}_{\Gamma}$.

6. Feasibility

The purpose of this section is to give an impression of the feasibility of this method as it applies to aircraft-mounted radiometers. The concern is whether radiometers can be expected to resolve the differences in (18).

Figure 17 shows profiles of horizontally averaged fractional differences between measured upwelling fluxes,

$$\Delta F \equiv \frac{F^{\uparrow}_{\lambda_2} - F^{\uparrow}_{\lambda_1}}{F^{\uparrow}_{\lambda_1}}(100\%), \tag{29a}$$

and downwelling radiances,

$$\Delta I \equiv \frac{I^{\downarrow}_{\lambda_2} - I^{\downarrow}_{\lambda_1}}{I^{\downarrow}_{\lambda_1}}(100\%), \tag{29b}$$

for Scene B at $\theta_0 = 60°$ with $\alpha_{\lambda_1} = 0.1$ and $\alpha_{\lambda_2} = 0.5$. The quantity ΔI is similar to Marshak et al.'s (2000) original NDCI. There should be little difficulty distinguishing upwelling fluxes near and below cloud base as ΔF are typically >500%. In fact, approximating domain-averaged $F^{\uparrow}_{\lambda}$ with the familiar geometric sum formula for internal reflections between surface and cloud (e.g., Wiscombe 1973; Schneider and Dickinson 1976), ΔF beneath cloud can be estimated as

$$\Delta F \approx \left\{\frac{\alpha_{\lambda_2}(1 - \alpha_{\lambda_1}A_c\langle\alpha_{\rm cld}\rangle)}{\alpha_{\lambda_1}(1 - \alpha_{\lambda_2}A_c\langle\alpha_{\rm cld}\rangle)} - 1\right\}(100\%)$$
$$\approx 525\%, \tag{30}$$

where $A_c = 0.89$ is cloud fraction (transparent clear sky), and $\langle\alpha_{\rm cld}\rangle \approx 0.54$ is spherical cloud albedo (Tables 1 and 4). Once in cloud, ΔF decreases rapidly, especially when τ above is relatively thick. This is because when cloud above is thick it is usually thick below too, so significant fractions of $F^{\uparrow}_{\lambda}$ (common to both λ) are due to cloud that masks the disparate surface source. Nev-

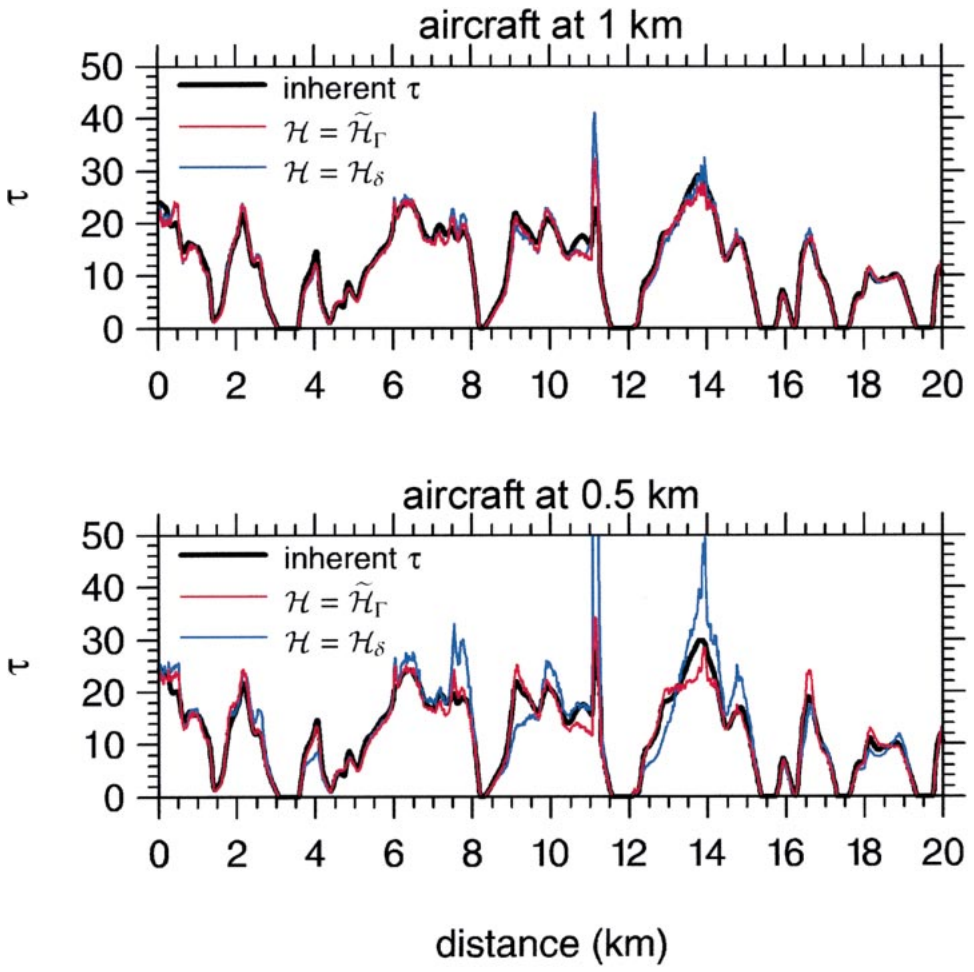

FIG. 15. A 20-km transect from Scene B showing inherent τ and τ' estimated by the aircraft method using both H_δ and $\tilde{H}_\Gamma$. Results are shown for transects at altitudes of 1 and 0.5 km.

ertheless, differences are typically >20% and should pose little difficulty.

For flights at most altitudes with τ aloft exceeding 5, values of ΔI are typically between 10% and 30% and should be resolvable by most radiometers. When τ aloft are less than 5, ΔI are generally between 5% and 10%. Moreover, for $\theta_0 = 60°$, $\alpha_{\lambda_1} = 0.1$, and $\alpha_{\lambda_2} = 0.5$, the limiting value of $\Delta I \approx 5\%$ near cloud top (i.e., $\tau \to 0$) was corroborated with DISORT. Given that radiometer integration periods will be short due to large aircraft speeds [e.g., 60 m s^{-1} for a Twin Otter and 100 m s^{-1} for a Convair 580 (J. W. Strapp 2001, personal communication)], these small values of ΔI may cause problems. While values shown in Fig. 17 are reduced slightly for $\theta_0 = 30°$, light levels are generally at least 70% larger than at 60° (i.e., $\cos 30°/\cos 60° = \sqrt{3}$).

The other factor influencing ΔF and ΔI is $\Delta\alpha \equiv \alpha_{\lambda_2} - \alpha_{\lambda_1}$. Although $\Delta\alpha = 0.4$, as used here, is not maximal (see Table 1), it is quite large. While the method presented here works in theory for small $\Delta\alpha$ (cf. BM2001), encounters with radiometer limitations can be expected for surfaces with little or no green vegetation. In these cases it is best to fly close to, or beneath, cloud base.

7. Summary and conclusions

The purpose of this paper was to introduce and assess a method for inferring cloud optical depth τ above some altitude z that uses data from radiometers mounted on an aircraft flying at z. This method was motivated by Marshak et al. (2000) and utilizes two similar wavelengths λ of radiation involved in multiple reflections between the atmosphere above z and the surface–atmosphere system below z. It is based on the assumptions that

1) average horizontal transport of upwelling diffuse radiation for real clouds can be approximated by 1D horizontal transport of upwelling isotropic radiation for homogeneous clouds [see Eq. (9)];

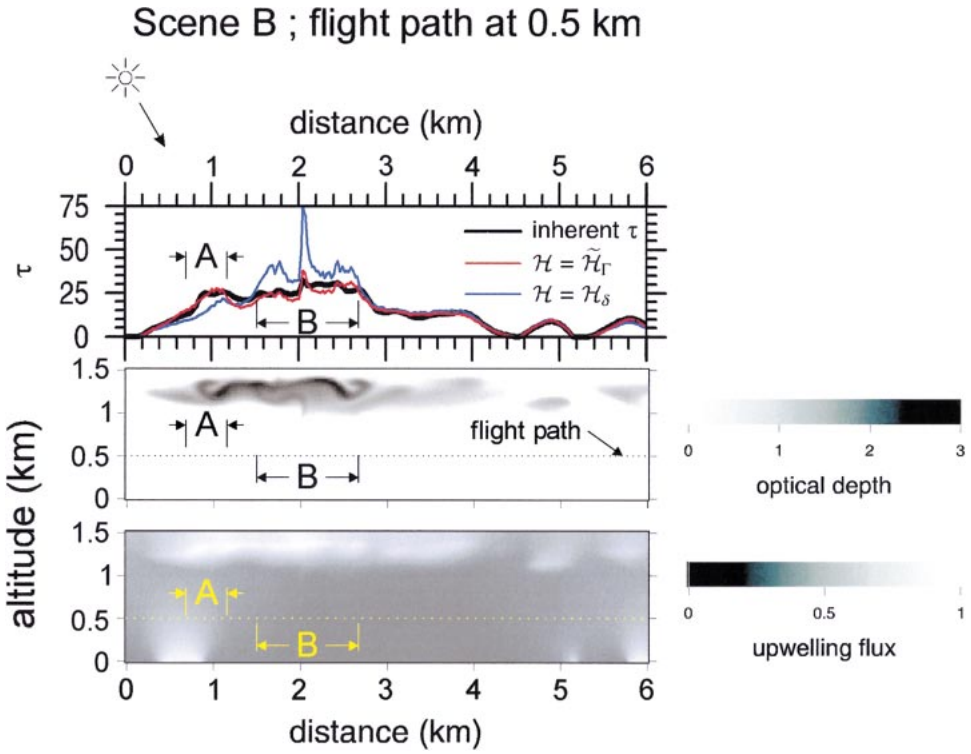

FIG. 16. Upper panel shows inherent and inferred τ for the first 6 km of the 11-km stretch of cloud in Scene B as shown in Fig. 3. Inferred values are for both $\tilde{H}_\Gamma$ and H_δ using data measured at an altitude of 0.5 km. The profile of τ is shown in the middle panel, and the lower panel shows a profile of upwelling flux for surface albedo of 0.5. Upper reaches of cloud and areas of direct-beam surface flux are identified readily as bright patches. Refer to the text for discussion of the ranges denoted by **A** and **B**.

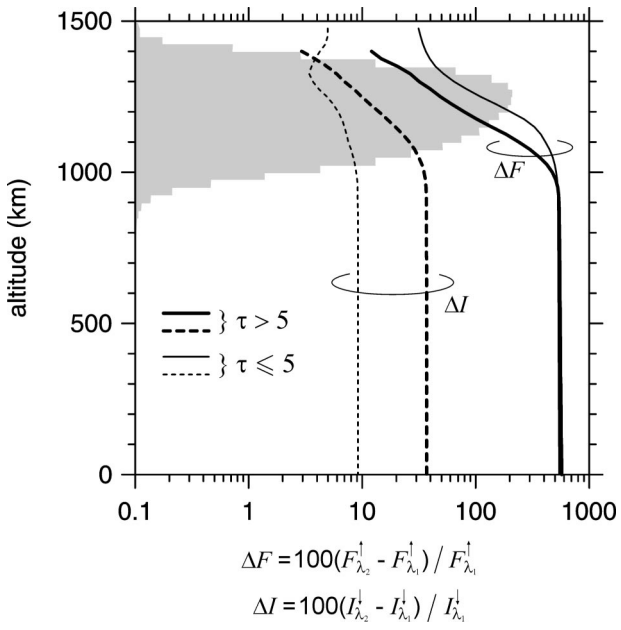

FIG. 17. Profiles of mean percentage differences between upwelling spectral fluxes $F^{\uparrow}_{\lambda}$ and downwelling spectral radiances $I^{\downarrow}_{\lambda}$ for Scene B at $\theta_0 = 60°$ using spectral surface albedos of 0.1 and 0.5. Separate profiles were computed depending on whether τ aloft was greater than or less than 5.

2) upwelling fluxes measured along an aircraft's trajectory L provide an adequate sample of the population across the entire plane parallel to earth that contains L [see Eqs. (14) and (17)]; and
3) optical properties at both λ are *similar* for the atmosphere above the aircraft but *differ* for the surface–atmosphere system beneath the aircraft.

The first assumption was found to be quite reasonable. Moreover, based on simulations performed here, violations of the assumption of isotropy appear to have minor impacts (see sections 4 and 5b). Violations of the second assumption are tempered by the fact that differences between upwelling fluxes (which tend to be very smooth at and above cloud base) at both λ are weighted by functions that decay away from the site of inference (see section 5a). The third assumption is satisfied particularly well for green vegetation. This method was compared to a related method that uses surface-based radiometric measurements (BM2001).

Some potential difficulties inherent in BM2001's surface-based technique are alleviated with an aircraft. Specifically, the surface method requires cloud-base fluxes based on time series of measured downwelling fluxes, which in turn, depend on estimates of cloud-base altitude, cloud advection rate, and local effective surface albedos. While their method works extremely

well under ideal conditions, it is at the mercy of cloud advection and the potential for poor sampling and anisotropic biases associated with advecting cloud. An aircraft flying in the vicinity of cloud base, however, moves quickly relative to cloud advection and evolution and, with a down-facing pyranometer, can measure upwelling flux directly over any surface type. Moreover, cloud and aerosol present beneath the aircraft are, in principle, not problematic. The primary drawbacks to the aircraft method are cost and limited application. Performing the operation from the surface can be inexpensive and data collection can be continuous and long-term (e.g., necessary instruments are being installed presently at the ARM-SGP site; C. Pavloski 2001, personal communication). Obviously the aircraft method will be used only during relevant field experiments.

The aircraft method uses an approximate, normalized radiative Green's function to refine initial estimates of τ. It was shown that for inhomogeneous boundary layer clouds, an analytic, horizontally and azimuthally averaged Green's function usually improves results. In particular, for flights beneath cloud base, a simple ballistic account of upwelling photon trajectories between aircraft and cloud base appears to work well. For very broken, cumuliform clouds, a more sophisticated approach is needed to deal with side illumination and leakage. Nevertheless, it is expected that estimates of τ will often satisfy most needs.

This method will provide a constraint (time series of τ) for more elaborate synergetic inversion techniques that utilize several measurements; for example, use of τ together with cloud water path from microwave radiometer data and millimeter cloud radar reflectivities to estimate profiles of cloud droplet concentration and effective radius (cf. Boers et al. 1998). In closing, it is noted that studies are in progress that focus on aircraft (and surface) applications of the method documented here to situations involving multilayer cloud fields, tropospheric aerosols, and realistic instruments.

Acknowledgments. This study was supported by grants from the U.S. Department of Energy's ARM Program [DE-FG02-90ER61071 to The Pennsylvania State University (PSU), DE-A105-90ER61069 to NASA/GSFC, and DE-FG02-97ER2361 to the Canada Centre for Remote Sensing]. A. Marshak was also supported by NASA's EOS Project Science Office at GSFC (under Grant NAG5-6675) as part of the EOS Validation Program. We thank B. A. Wielicki (NASA/Langley) for making computer time available; E. E. Clothiaux, A. B. Davis, Y. Knyazikhin, C. F. Pavloski, and W. J. Wiscombe for helpful discussions; and W. Evans for the loan of the spectrometer.

REFERENCES

Barker, H. W., 1995: Reassessing the elliptic phase function for use in two-stream approximations. *J. Atmos. Sci.,* **52,** 2227–2231.

——, and Z. Li, 1997: Interpreting shortwave albedo-transmittance plots: True or apparent anomalous absorption. *Geophys. Res. Lett.,* **24,** 2023–2026.

——, and A. Marshak, 2001: Inferring optical depth of broken clouds above green vegetation using surface solar radiometric measurements. *J. Atmos. Sci.,* **58,** 2989–3006.

——, T. J. Curtis, E. Leontieva, and K. Stamnes, 1998: Optical depth of overcast cloud across Canada: Estimates based on surface pyranometer and satellite measurements. *J. Climate,* **11,** 2980–2994.

Boers, R., H. W. J. Russchenberg, and J. S. Erkelens, 1998: Ground-based remote sensing of stratocumulus cloud droplet concentration during CLARA-1996. International Research Centre for Telecommunication-transmission and Radar (IRCTR), Delft University of Technology Rep. IRCTR-S-023-98, 23 pp.

Brenguier, J.-L., and W. W. Grabowski, 1993: Cumulus entrainment and cloud droplet spectra: A numerical model within a two-dimensional dynamical framework. *J. Atmos. Sci.,* **50,** 120–136.

Cahalan, R. F., W. Ridgway, W. J. Wiscombe, T. L. Bell, and J. B. Snider, 1994: The albedo of fractal stratocumulus clouds. *J. Atmos. Sci.,* **51,** 2434–2455.

Davis, A. B., A. Marshak, R. F. Cahalan, and W. J. Wiscombe, 1997: The Landsat scalebreak in stratocumulus as a three-dimensional radiative transfer effect: Implications for cloud remote sensing. *J. Atmos. Sci.,* **54,** 241–260.

Gultepe, I., G. A. Isaac, and K. B. Strawbridge, 2001: Variability of cloud microphysical and optical parameters obtained from aircraft and satellite remote sensing during RACE. *Int. J. Climatol.,* **21,** 507–525.

Han, Q., W. B. Rossow, J. Chou, and R. M. Welch, 1998: Global survey of the relationships of cloud albedo and liquid water path with droplet size using ISCCP. *J. Climate,* **11,** 1516–1528.

Harshvardhan, B. A. Wielicki, and K. M. Ginger, 1994: The interpretation of remotely sensed cloud properties from a model parameterization perspective. *J. Climate,* **7,** 1987–1998.

Henyey, L. C., and J. L. Greenstein, 1941: Diffuse radiation in the galaxy. *Astrophys. J.,* **93,** 70–83.

Joseph, J. H., W. J. Wiscombe, and J. A. Wienman, 1976: The delta-Eddington approximation for radiative transfer. *J. Atmos. Sci.,* **33,** 2452–2459.

Kimes, D. S., 1983: Dynamics of directional reflectance factor distributions for vegetation. *Appl. Opt.,* **22,** 1364–1372.

——, W. W. Newcomb, R. F. Nelson, and J. B. Schutt, 1986: Directional reflectance distribution of a hardwood and pine forest canopy. *IEEE Trans. Geosci. Remote Sens.,* **24,** 281–283.

Knyazikhin, Y., and A. Marshak, 2000: Mathematical aspects of BRDF modeling: Adjoint problem and Green's function. *Remote Sens. Rev.,* **18,** 263–280.

Leontieva, E., K. Stamnes, and J. A. Olseth, 1994: Cloud optical properties at Bergen (Norway) based on the analysis of long-term solar irradiance records. *Theor. Appl. Climatol.,* **50,** 73–82.

Leontyeva, E., and K. Stamnes, 1994: Estimations of cloud optical thickness from ground-based measurements of incoming solar radiation in the arctic. *J. Climate,* **7,** 566–578.

Li, Z., A. Trishchenko, H. W. Barker, G. L. Stephens, and P. Partain, 1999: Consistency analyses of ARESE and satellite measurements for studying cloud absorption. *J. Geophys. Res.,* **104,** 19 127–19 134.

Lyapustin, A., 1999: Atmospheric and geometrical effects on land surface albedo. *J. Geophys. Res.,* **104,** 4127–4144.

Marchuk, G. I., G. A. Mikhailov, M. A. Nazaraliev, R. A. Darbinjan, B. A. Kargin, and B. S. Elepov, 1980: *Monte Carlo Methods in Atmospheric Optics.* Springer-Verlag, 208 pp.

Marshak, A., A. B. Davis, W. J. Wiscombe, and R. F. Cahalan, 1995a: Radiative smoothing in fractal clouds. *J. Geophys. Res.,* **100,** 26 247–26 261.

——, ——, ——, and G. Titov, 1995b: The verisimilitude of the independent pixel approximation used in cloud remote sensing. *Remote Sens. Environ.,* **52,** 72–78.

——, ——, ——, W. Ridgway, and R. F. Cahalan, 1998: Biases in shortwave column absorption in the presence of fractal clouds. *J. Climate,* **11,** 431–446.

——, Y. Knyazikhin, A. B. Davis, W. J. Wiscombe, and P. Pilewskie, 2000: Cloud–vegetation interaction: Use of Normalized Difference Cloud Index for estimation of cloud optical thickness. *Geophys. Res. Lett.,* **27,** 1695–1698.

Min, Q., and L. C. Harrison, 1996: Cloud properties derived from surface MFRSR measurements and comparison with GOES results at the ARM SGP site. *Geophys. Res. Lett.,* **23,** 1641–1644.

Minnis, P., P. W. Heck, D. F. Young, C. W. Fairall, and J. B. Snider, 1992: Stratocumulus cloud properties from simultaneous satellite and island-based instrumentation during FIRE. *J. Appl. Meteor.,* **31,** 317–339.

Mitchell, J. F. B., R. A. Davis, W. J. Ingram, and C. A. Senior, 1995: On surface temperature, greenhouse gases, and aerosols: Models and observations. *J. Climate,* **8,** 2364–2386.

Myneni, R. B., and G. Asrar, 1993: Radiative transfer in three-dimensional atmosphere–vegetation media. *J. Quant. Spectrosc. Radiat. Transfer,* **49,** 585–598.

Schneider, S. H., and R. E. Dickinson, 1976: Parameterization of fractional cloud amounts in climate models: The importance of modelling multiple reflections. *J. Appl. Meteor.,* **15,** 1050–1056.

Slingo, A., 1989: A GCM parameterization for the shortwave radiative properties of water clouds. *J. Atmos. Sci.,* **46,** 1419–1427.

Stamnes, K., S.-C. Tsay, W. J. Wiscombe, and K. Jayaweera, 1988: A numerically stable algorithm for discrete-ordinate-method radiative transfer in multiple scattering and emitting layered media. *Appl. Opt.,* **27,** 2502–2509.

Stephens, G. L., and C. M. R. Platt, 1987: Aircraft observations of the radiative and microphysical properties of stratocumulus and cumulus cloud fields. *J. Climate Appl. Meteor.,* **26,** 1243–1269.

Stokes, G. M., and S. E. Schwartz, 1994: The Atmospheric Radiation Measurement (ARM) program: Programmatic background and design of the cloud and radiation test bed. *Bull. Amer. Meteor. Soc.,* **75,** 1201–1221.

Szyrmer, W., and I. Zawadzki, 1999: Modeling of the melting layer. Part I: Dynamics and microphysics. *J. Atmos. Sci.,* **56,** 3573–3592.

Tucker, C. J., 1979: Read and photographic infrared linear combination for monitoring vegetation. *Remote Sens. Environ.,* **8,** 127–150.

Verstraete, M. M., and B. Pinty, 1996: Designing optical spectral indices for remote sensing applications. *IEEE Trans. Geosci. Remote Sens.,* **34,** 1254–1265.

Wiscombe, W. J., 1973: Solar radiation calculations for Arctic stratus conditions. *Climate of the Arctic: 24th Alaska Science Conference, August 1973,* G. Weller and S. A. Bowling, Eds., Geophysical Institute 245–254.

——, and G. W. Grams, 1976: The backscattered fraction in two-stream approximations. *J. Atmos. Sci.,* **33,** 2440–2451.